Training and Communication for Earthquake Risk Assessment

TREQ Project

Probabilistic seismic hazard model for the Dominican Republic

Deliverable 2.2.2 – Version 2.1.0

Global Earthquake Model (GEM) Foundation

www.globalquakemodel.org

Description of the probabilistic seismic hazard model developed for the Dominican Republic

Deliverable D2.2.2 – Probabilistic seismic hazard model for the Dominican Republic

Deliverable D2.2.2

Technical report produced in the context of the TREQ project

Version 2.1.0 – June, 2022

Kendra Johnson[1], Marco Pagani[1], Thomas Chartier[1]

[1]Global Earthquake Model (GEM) Foundation

Collaborators

The authors would like to our collaborators in the Dominican Republic for their invaluable contribution to the project, including but not limited to collecting local data, organizing meetings and communicating the results to stakeholders and the general public.

The authors would like in particular to thank the following partners for their support:

- Servicio Geológico Nacional (SGN) de la República Dominicana, especially Yesica Perez, Vladimir Guzmán, Maria Betania Roque Quezada, Freddy Guzmán, Edwin Garcia and Santiago Muñoz (former director).
- Universidad Autónoma de Santo Domingo (UASD), especially Ramon Delanoy.
- Instituto Sismológico Universitario.

Other contributors

Robin Gee, Richard Styron, Catalina Yepes-Estrada, Michele Simionato, Shreyasvi Chandrasekhar, and Manuela Villani from the Global Earthquake Model (GEM) Foundation

Authors of previous versions

Julio Garcia-Pelaez (formerly at the GEM Foundation)

Acknowledgements

This report forms part of the United States Agency for International Development (USAID) and the Bureau of Humanitarian Assistance (BHA) funded program for Training and Communication for Earthquake Risk Assessment (TREQ) project, grant AID-OFDA-G-720FDA19GR00273. The Global Earthquake Model Foundation manage and executes the resources of USAID and implements the project in collaboration with local stakeholders.

The TREQ Project is designed to demonstrate how earthquake hazard and risk assessment can inform decision makers in the development of risk reduction policies, as well as how earthquake risk can be properly communicated to stakeholders and the public in general. Specifically, the project aims to develop capacity for urban earthquake risk assessment in Latin America, Quito (Ecuador), Cali (Colombia), and Santiago de los Caballeros (Dominican Republic), while the second part will produce training, educational and communication materials that will enhance the understanding of earthquake risk worldwide. This program targets a wide spectrum of stakeholders, categorized into four main groups: governance (decision-makers/public authorities), industry (practitioners and professionals), academia (researchers and professors), and the community.

This report has been made possible thanks to the support and generosity of the American people through the United States Agency for International Development (USAID) and the Bureau of Humanitarian Assistance (BHA). The opinions, findings, and conclusions stated herein are those of the authors and do not necessarily reflect the views of USAID or the United States Government.

Citation: Johnson. K., Pagani M., Chartier, T. (2022) Probabilistic seismic hazard model for the Dominican Republic D.2.2.2, v2.1.0, June 2022.

Table of Contents

1 INTRODUCTION

The "urban hazard" component of the TREQ project aimed to assess earthquake shaking hazard at an urban scale for three major urban centers in Latin America: Quito, Ecuador; Cali, Colombia, and Santiago de los Caballeros, Dominican Republic. The first task was to conduct a critical review of the available probabilistic seismic hazard assessment (PSHA) models covering each of the selected cities and to choose a reference PSHA model to be used for rock and soil calculations (see more details in the TREQ technical report *"D2.2.1 Description of the compiled datasets and the selected seismic hazard models"*). For the Dominican Republic, we reviewed the following documents and products:

- Caribbean and Central America Risk Project (CCARA): GEM Foundation's Global Hazard Mosaic (Pagani et al., 2020b) covers the Dominican Republic with an updated version of the PSHA model developed within the CCARA project. This model is freely available for public-good applications, and implemented in the OpenQuake Engine format. However, the model has regional coverage, and thus does not account for epistemic uncertainties in the source model at a level suitable for urban hazard analysis.
- Seismic Hazard Maps for Haiti by Frankel et al. (2011): part of the Dominican Republic is covered by the model used to develop these maps. However, the model does not account for all of the sources that could affect the eastern part of the Dominican Republic.
- Microzonificación sísmica de Santiago de los Caballeros - República Dominicana Amenaza sísmica regional by Bertil et al. (2010): This microzonation study covers the city of Santiago in detail, but does not provide the same detailed coverage of the full island.
- Dominican Republic building code: a seismic zonation and hazard maps were developed as a part of the Dominican Republic building code (R-001, 2011; "Reglamento para el Análisis y Diseño Sísmico de Estructuras"). However, there is no technical documentation about the PSHA study (model) used.
- Active fault characterization and seismotectonic zoning of the Hispaniola Island by Terrier-Sedan and Bertil (2021): This publication proposes a seismic source model for the full island of Hispaniola. The model is not yet implemented in a PSHA software but is a useful resource for seismotectonic information in the study region.

While each of the above is an invaluable resource for understanding the seismic hazard in Santiago de los Caballeros and the whole of the Dominican Republic, none were deemed suitable for in the TREQ project, either because they lacked sufficient consideration of epistemic uncertainties for use in the urban hazard application; because the source models are not publicly available; or because they do not fully coverage the Dominican Republic and thus any future urban hazard applications for other cities may be prohibited. Instead, GEM Foundation used these resources and collaborated with local institutions (Servicio Geológico Nacional, SGN; Universidad Autónoma de Santo Domingo, UASD) to develop a national model. Furthermore, the final results will be compared to those of the studies listed above.

To develop the probabilistic seismic hazard model for the Dominican Republic, we mostly followed the model-building workflows that are standardly used by GEM; however, we also incorporated some newer methodologies that we consider more robust. This document describes the development of a national PSHA model for the Dominican Republic, herein called the **DOM21** model. The first section

introduces the seismotectonics of the Dominican Republic. The second section describes the major datasets that were used to build the model, including an ad-hoc homogenized catalogue compiled as part of the project. The third section describes the seismic source characterization, including the analyses performed alongside in order to validate the model components. The fourth section describes the seismic attenuation properties of Hispaniola and the ground motion model logic tree that was selected for DOM21. The fifth section presents the main seismic hazard results computed from the model using the OpenQuake Engine, focusing mostly on the city of Santiago de los Caballeros. The final section discusses how the results compare to those of former models, and thus how this study has changed our understanding of seismic hazard in the Dominican Republic.

1.1 Seismotectonic setting of the Dominican Republic

The Dominican Republic occupies the eastern part of Hispaniola Island, which is part of the Greater Antilles archipelago. The island is located in a complex tectonic environment at the northeastern extent of the Caribbean (CARIB) plate near its boundary with the North American (NOAM) plate (Mann et al., 2005; Pindell and Kennan, 2009; Demets et al., 2010; Benford et al., 2012, Rodriguez-Zurruno et al., 2020). The CARIB plate moves east-north-eastward at a rate of 18 – 20 mm/year relative to the North America Plate (DeMets et al., 2000), which results in complicated subduction tectonics at the plate boundary. In Hispaniola, the NOAM subducts obliquely under the CARIB, resulting in both oblique convergence at the subduction interface north of Hispaniola and Puerto Rico, as well as strike-slip faulting to the south of the plate boundary.

The complexity of the plate boundary in this area has resulted in several interpretations of the subduction geometry and segmentation as well as the shallow structures accommodating oblique convergence. However, the microplate oblique collisional model proposed by Mann et al. (2002), based on GPS and geologic data, is widely accepted and has been used in numerous studies (i.e., Benford et al., 2012; Calais et al., 2016). In this model, depicted in Figure 1, the region is divided into several microplates and tectonic blocks (i.e., the Gonave, Septentrional, Hispaniola and Puerto Rico - Virgin Islands), which is more consistent with GPS measurements and geologic data than some of the simpler models (e.g., Mann et al., 1984).

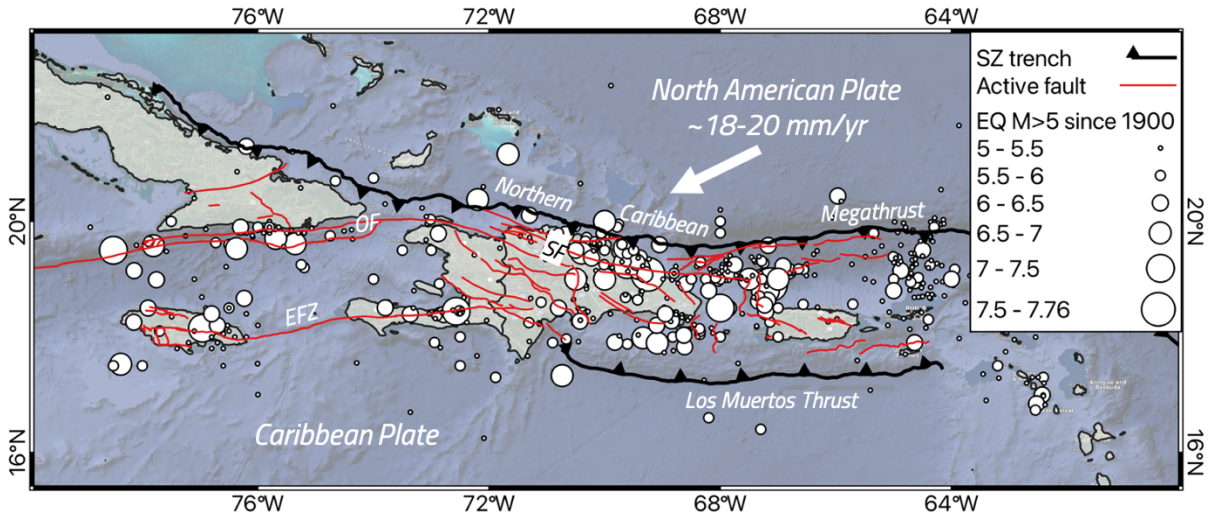

Figure 1 Overview of the northern Caribbean-North American plate boundary zone, indicating some major structures. Earthquake positions are from the DOM21 catalogue developed herein. Subduction zone (SZ) traces from the ***Global Active Faults Database*** *(GAF-DB; Styron and Pagani, 2020). Other active faults from the SGN database described in the text (e.g. Bertil et al., 2015 and further communication). OF: Oriente fault. SF: Septentrional fault. EFZ: Enriquillo-Plantain Garden Fault Zone.*

In Hispaniola, the plate motion is partitioned between shortening and strike-slip faulting. The shortening occurs on folds and thrusts in the central part of the Island, forming mountain ranges and valleys such as the Massif de la Selle in Haiti and the Central Cordillera in the Dominican Republic). This region, known as the Hispaniola microplate (or block), is bounded by two left-lateral strike-slip fault systems: the Septentrional Fault (SFZ) to the north and the Enriquillo-Plaintain Garden Fault (EFZ) to the south.

Seismicity occurring near the plate boundary includes large events of both crustal and subduction origin. Historically, several significant earthquakes have impacted the Dominican Republic, including a 16th century event near Santiago de los Caballeros, 1751 earthquake on the Enriquillo-Plantain Garden fault system, and a 1770 event in the Los Muertos Trough. Haiti also experienced two significant events in 1842 and 1887. More recently, a series of six large subduction earthquakes struck the North Hispaniola Trench to the north of the Dominican Republic between 1943 and 1953, the largest being the 1946 M_W 7.76 earthquake; this event, which is the largest instrumentally recorded earthquake to impact the island, also triggered a tsunami. In 2010, the highly consequential M_W 7.0 Haiti earthquake struck the southwestern part of Hispaniola. This event was associated to a secondary structure of the Enriquillo-Plantain Garden Fault System, the Léogâne fault (Calais et al., 2010), and confirmed the seismogenic potential of the island's major faults and their need to be explicitly considered in hazard analyses. Most recently, in August 2021, another highly damaging earthquake of M_W 7.2 struck to the west on this fault system.

Most of the recorded seismicity in Hispaniola is shallower than ~40 km and occurs on the structures that accommodate the oblique convergence. Intermediate and deep events also occur within the slab of the down-going NOAM plate along the Puerto Rico and North Hispaniola trenches, as well as the Los Muertos trench southeast of the island, and extend to around 250 km depth.

2 DATA COLLECTION AND COMPILATION OF BASIC DATASETS

In addition to information gathered from the former studies on seismic hazard in the Dominican Republic, and other publicly available tectonic information, we relied on two primary datasets to build DOM21: (1) a homogenized earthquake catalogue, and (2) an active fault database, both covering Hispaniola and its surroundings.

2.1 Homogenized Earthquake Catalogue

A homogenized earthquake catalogue is an important dataset used for most seismic hazard studies. A robust earthquake catalogue is necessary for developing the seismic source characterization, as it indicates where and how frequently earthquakes are occurring in the region of interest. "Homogenized" indicates that information from multiple earthquake databases covering the region has been combined to produce a single catalogue, ensuring that a constant magnitude scale is used throughout; that only a single entry is included for each earthquake that occurred, and that the selection of earthquake parameters from events with duplicated entries follows a hierarchical procedure assigned to the original databases. A homogenized catalogue was constructed during the TREQ project to use in developing the DOM21 PSHA model, following the approach proposed in Weatherill et al. (2016) and using the OpenQuake Catalogue Toolkit (OQ-CATK[1]): an open-source Python toolkit developed by GEM. The OQ-CATK workflow used herein takes the following steps:

(1) Collect available earthquakes catalogues and bulletins covering Hispaniola plus a buffer that covers all seismic sources within ~300 km of the island and merge them into a single database
(2) Duplicates are identified by matching earthquake records within the database that have similar origin times and hypocenters
(3) Choose one record from each set of duplicates based on a hierarchy of reporting agencies and magnitude types, purging the others from the database
(4) Convert all selected magnitudes into a common unit

The Dominican Republic is already covered by the catalogue developed within the Central America and the Caribbean (CCARA) project (Garcia and Poggi, 2017a), and so the catalogue developed within TREQ benefits significantly from the former effort. However, because the new catalogue focuses on a smaller region, the hierarchies used give more prevalence to the agencies that oversee local station.

2.1.1 Developing the earthquake database

Step (1) merged the publicly available earthquake catalogues as well as data provided by agencies in the Dominican Republic within the TREQ project. Table 1 lists the sources of earthquake origins included in the merged database, the number of contributions from each, and their date and magnitude coverages. Most of these agencies are accessed through the ISC (Boletín del Centro Sismológico Internacional). While the catalogue compiled during the CCARA project, denoted as agency "CCA", is directly included in the database, the original data sources still are sometimes included. This is because

[1] https://github.com/GEMScienceTools/oq-mbtk/tree/master/openquake/cat

during CCARA, there were some instances of agencies for which there were insufficient pairings with another agency, and therefore robust magnitude conversions (described more below) were not possible; however, with more data available for the present study, we can reconsider some conversion possibilities.

We agencies listed in Table 1 come from the following catalogues or databases:

- CCA catalogue: Garcia and Poggi (2017), developed in the CCARA project and covering the Caribbean and Central America
- Bulletins of the Servicio Sismológico Nacional of Mexico (SSNC): a subset of the CCA catalogue that was separated because during the CCA effort, no conversion equation was developed for the SSNC magnitudes. This bulletin includes some events occurring in the western part of the region used here.
- International Seismological Center (ISC) bulletin extending through 30 November 2018 (the latest possible date at the time of download). Agencies accessed through ISC are marked with an asterisk (*) in Table 1. The ISC has global coverage.
- ISCGEM catalogue version 7.0 (Note: the extended version compiled by Weatherill et al. (2016) was used to construct the CCA catalogue). ISCGEM has global coverage.
- Global Centroid Moment Tensor (GCMT) catalogue: (GCMT, Ekström et al., 2012), ranging from 1976 to the end of 2018, is the most accurate collection of moment tensor solutions ($M_W \geq 5$). GCMT has global coverage.
- UASD-SGN catalogue: the catalogue of the Dominican Republic's local agencies Servicio Geológico Nacional (SGN) and Universidad Autónoma de Santo Domingo (UASD). Events cover Hispaniola Island and surroundings and extend from 1916 through 2019.

Using the OQ-CATK, the bulletins are all merged into a single database, where step (2) is performed. The entries are treated as duplicates if their origins match to within 0.5° and 40 s; the database then stores each entry as a single event but with multiple origins and magnitudes. This windowing is not always sufficiently coarse for the oldest events, and so a second, semi-automated check for duplicates is performed later in the workflow.

Table 1 Data used to construct the homogenized catalogue used herein. Agency codes correspond to those listed in the Bulletin of the ISC.[2]

Agency	Num Origins	Min Year	Max Year	Min Mag	Max Mag
IDC*	7410	2000	2018	1.7	7.1
CCA	7108	1678	2016	3.01	7.8
NEIC*	6115	1985	2018	1.4	7.6
SSNC	6115	1904	2018	0	7.6
RSPR*	5112	2001	2018	2	6.5
ISC*	2511	1918	2018	2.7	7.7
TRN*	1214	1961	2018	1.6	6.6
UASD	1087	1916	2019	4	7.7
JSN*	551	2000	2018	1.5	6.4
BJI*	317	1988	2018	4	7.7
OSPL*	302	2013	2018	1.3	6.1
SDD*	292	2009	2018	1.2	5.8
MOS*	262	1962	2018	4	7.1
NEIS*	255	1971	1984	3.2	6.9
EIDC*	232	1995	2000	2.6	5.4
GCMT	193	1970	2018	4	7
USCGS*	160	1964	1970	3.6	5.8
GCMT	141	1977	2017	4.8	7.1
ISCGEM	105	1905	2014	4.98	7.76
LDG*	105	1999	2010	3.2	6.5
SZGRF*	53	2006	2010	4	7.2
LAO*	48	1966	1975	3.5	6.1
GUTE*	47	1911	1948	6.6	8.1
IASPEI*	22	1964	2004	4	5.5
BGR*	22	2010	2018	4.3	6.8

2.1.2 Magnitude and origin selection hierarchy and homogenization

In step (3), the OQ-CATK uses a set of user-defined hierarchies to select a single origin and magnitude for each entry, which will ultimately be included in the catalogue for the Dominican Republic. Here, we used the following assumptions in order to define the hierarchy.

- Because the UASD-SGN bulletin is operated by national agencies of the Dominican Republic, we used this catalogue with a high level of confidence.
- Reviewed catalogues are assumed to have more reliable origins

[2] http://www.isc.ac.uk/iscbulletin/agencies/

- The final catalogue will use moment magnitudes (M_W), and so magnitudes that are natively reported on this scale will be prioritized. Other magnitudes will be converted whenever possible in step (4).

To better understand how the UASD catalogue compares to the reviewed global catalogues, we used magnitude density plots that compare the magnitudes computed by two agencies for a single event (i.e., Figure 2). We found that the M_W defined by UASD are approximately equal to the M_W from ISCGEM and the GCMT. Following this, we set the following generalized hierarchy:

(1) The most reliable magnitudes are those that are natively M_W.
(2) The next-best option is a magnitude for which a conversion relationship to M_W has been developed from large, global datasets (e.g., Weatherill et al., 2016).
(3) If these are unavailable, we will aim to use ad-hoc conversion equations, and thus choose magnitude types for which there are many entries with a preferred magnitude, and thus for which a robust ad-hoc conversion can be developed.
(4) The last-choice magnitudes are those for which there are not enough overlapping events to convert independently. Table 2 shows the magnitude hierarchy used to select earthquake magnitudes. (Note: when the CCA catalogue was added the database, the reporting agencies and magnitude types originally used to build the CCA catalogue were used for these field in the entries, rather than being assigned the agency id "CCA".)

Once the set of magnitudes for each event has been selected, the final step is to convert all magnitudes into the same M_W measure. To do so, we produced magnitude-agency density plots, as in Figure 2, aiming to find pairings for each non-M_W magnitude with sufficient events to determine a conversion equation. First, we use magnitude conversions that were developed by Weatherill et al. (2016) using global datasets, visually checking that these equations hold true for the subset of events in the DOM21 database. When these are unavailable, we develop our own. The final equations are in Table 3.

In order to pick one earthquake origin from the database, we aimed to treat the UASD catalogue as the dominant catalogue to the extent possible, as for magnitude. We deemed UASD first in the location hierarchy; followed by SSNC (also a local/regional network); CCA locations for which local or regional catalogues were prioritized; ISCGEM; and then the ISC prime.

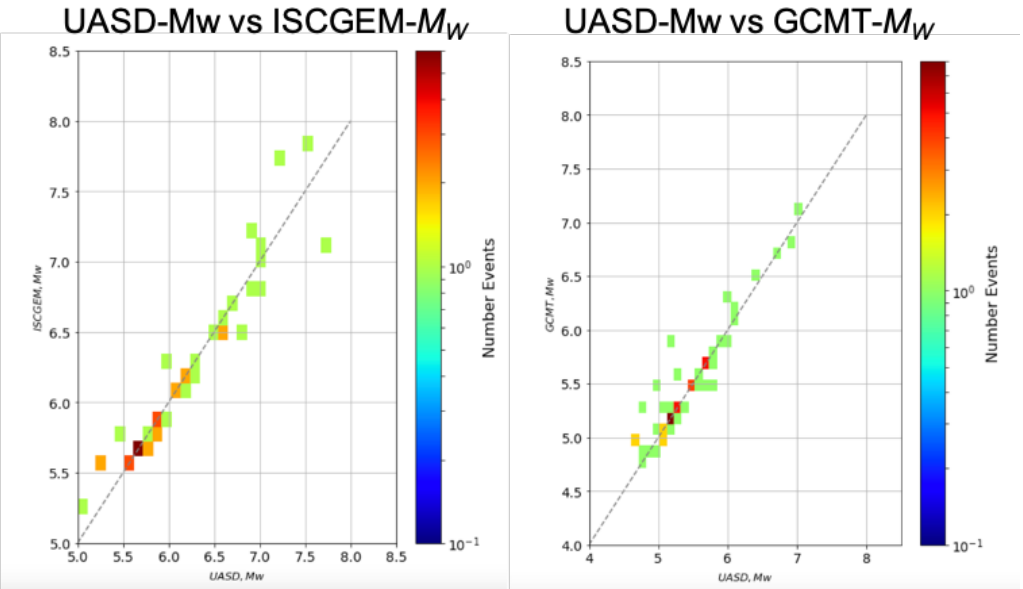

Figure 2 Magnitude-agency density plots showing that UASD-Mw is comparable to Mw from other agencies.

Table 2 Hierarchy of magnitudes and magnitude types used to produce the homogenized catalogue.

Magnitude type, description	**Hierarchy:** Agency (magnitude type)
M_w* and *M_W from global or local catalogues	GCMT (M_w/M_W), ISCGEM (M_w), **UASD (*M_w*)**, NEIC (M_{Wr}), SSNC (M_w/M_W)
M_S* and *m_b from agencies with conversion equations defined by Weatherill et al. (2016)	ISC (M_S), ISC (m_b), NEIC (m_b), IDC (m_b)
Other magnitudes either with ad-hoc conversions or kept in their native scale	RSPR (M_D), OSPL (M_L), all other (M_w/M_W, *UK*, M_S, M_D, m_b, M_L, m_d, M_t)

The magnitude frequency distribution (MFD) of the final DOM21 catalogue is shown in Figure 3. We resolved a Gutenberg-Richter negative exponential MFD with *a*-value = 6.086 and *b*-value = 1.059.

Table 3 Conversion equations used to compute among the different magnitudes (type and agency).

Agency (type)	**Conversion equation**
GCMT, ISCGEM, UASD, SSNC, CCA (M_w/M_W)	*No conversion**
NEIC (M_{Wr})	*Weatherill et al. (2016)* linear*
ISC (m_b)	*Weatherill et al. (2016)* linear*
ISC (M_S)	*Weatherill et al. (2016)* 2-segment*
NEIC (m_b)	*Weatherill et al. (2016)* 2-segment*
IDC (m_b)	$0.604 + 0.979m_b$ (ad-hoc from 406 events)

RSPR (M_D)	0.5546 + 8878M_D (ad-hoc from 474 events)
OSPL (M_L)	M_L >= 5.0: -1.731 + 1.298M_L M_L < 5.0: 2.193 + 0.513M_L (ad-hoc from 128 events)
All other (M_w/M_W, *UK*)	*No conversion*[*]
All other (M_S)	2.1336 + 0.6497M_S (ad-hoc from 375 events: IDC, MOS, BJI, EIDC, NEIS, PAS)
All other (M_D)	1.6312 + 0.6287M_D (ad-hoc from 186 events: JSN, SSNC, SDD, TRN)
All other (m_b)	0.8222 + 0.8302m_b (ad-hoc from 213 events: BGR, MOS, IASPEI, EIDC, NEIS, TRN)
All other (M_L)	0.7250 + 0.9369M_L (ad-hoc from 453 events: IDC, SDD, RSPR, SSNC)
All other (m_d)	*No conversion* (ad-hoc)
All other (M_t)	0.1911 + 0.9874M_t (ad-hoc from 30 events: TRN)

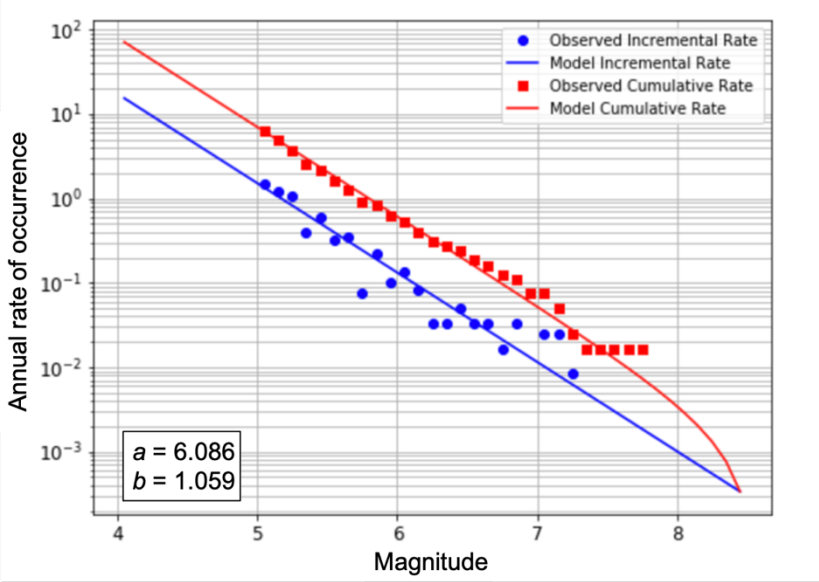

Figure 3 MFD for the final DOM21 catalogue. Blue is observed incremental observations (points) and the best-fit Gutenberg-Richter MFD (line), and red is observed cumulative rate (squares) and GR MFD

As a final catalogue quality check, we searched the catalogue for any possible remaining duplicates that were not accounted for in the initial merging. The check used 0.3 ° and 10 s spatial and time search windows. 183 possible duplicated events are identified; however, all candidates (with one exception) are pairs of events that *both* are derived from the UASD catalogue. Furthermore, only three correspond to events M_W>5. We do not consider these events to be duplicates and therefore do not exclude any from the final catalogue. The exception is a pair of events from 1927 that both appear in the CCA catalogue; one comes from ISCGEM (M~5.7) and the other from ISCGEM-extended (M~6.5). We were unable to find other evidence of the larger event, and therefore kept the *M* 5.7 event.

2.1.3 Tectonic regionalization of seismicity

The workflow used herein to perform the seismic source characterization, and in particular the use of seismicity to constrain occurrence rates for many of the sources, requires that the earthquake

catalogue has been classified to the tectonic regimes that affect the seismic hazard. For example, the occurrence rates of sources occurring in the down-going slab should be constrained using only seismicity that is thought to have occurred within that slab. We used the procedure of Pagani et al. (2020a) to classify the catalogue created herein. This procedure, implemented in GEM's OpenQuake Model Building Toolkit (MBTK[3]), classifies an earthquake according to the proximity of its hypocenter to reference surfaces used to delineate the tectonic regions.

In the DOM21 model, we classify the hypocenters to four tectonic domains: (1) active shallow crust, (2) the subduction interface of the Puerto Rico Trench, (3) subduction intraslab of the Puerto Rico Trench, and (4) subduction intraslab of the North Hispaniola Trench. While the North Hispaniola Trench and Los Muertos Trench subduction interfaces are also considered to be independent tectonic region types in the seismic source characterization, there are too few earthquakes in either domain to be used to constrain the occurrence rates; thus, earthquakes that were caused by these sources are classified as crustal in this stage, however, the relevant sources are ultimately modelled as subduction interfaces (this is explained more thoroughly with the Seismic Source Characterization). Additionally, the Los Muertos Trench is sometimes considered a shallow thrust belt rather than a plate boundary, and the geometries of both structures are poorly constrained; thus, it is useful to include them in the crustal modelling workflow so that some of the seismicity is distributed off the primary surfaces.

The classification algorithm used the following assumptions and surfaces, defined specifically for this application, to assign each earthquake to a tectonic domain.

(1) Moho depths from Lithos 1.0 are (Pasayanos et al., 2014) used to define the lower depth threshold of crustal seismicity. Hypocenters shallower than the Moho depth plus a 40 km buffer are classified as crustal. Note that a very large buffer that ensures earthquakes occurring on the LMT or NHT are included; however, the hierarchy applied later ensures that this does not cause earthquakes in the PRT interface or the slabs to be labeled as crustal, and in the crustal modelling steps, earthquakes shallower than 50 km are not considered.
(2) Slab2.0 (Hayes et al., 2018) is used to define a surface representing the PRT interface; hypocenters occurring within 10 km above and 30 km below the surface, and shallower than 60 km depth are classified to this domain.
(3) Slab2.0 is also used to define the top of the PRT slab volume. Earthquakes occurring within 20 km above and 50 km below this surface are classified as PRT intraslab.
(4) The seismic source characterization of Terrier-Sedan and Bertil (2021) is used to define the top of the NHT slab volume, but with the upper depth limit increased from 25 km to 40 km. The same buffers and depth thresholds as in (3) are used to assign earthquakes to this slab. The remaining hypocenters are left unclassified.

In some cases, the classification results indicate that an earthquake could have occurred in multiple tectonic regions. For example, some events are both shallower than the Moho *and* within 20 km of the

[3] https://github.com/GEMScienceTools/oq-mbtk

PRT interface. In these cases, a hierarchy is used to determine which tectonic domain should be assigned. Here, earthquakes are considered more likely to occur in the slab than the active shallow crust, and more likely to originate on the interface than within the slab. Finally, the largest events – those $M_W > 6.5$ and within the completeness thresholds used in the seismic source characterization (see next sections) are manually inspected and compared to historical records, and events that we deem to be misclassified are reassigned to their correct domain. In this case, we reassigned two earthquakes: a 1947 M_W 7.7 to the PRT interface; and a 1979 M_W 6.7 to the NHT intraslab. We also removed a 2012 M_W 6.5 event coming from the UASD catalogue that was not included in other catalogues.

The final classification assigned 815 earthquakes to the NHT intraslab, 429 to the PRT intraslab, 2303 to the PRT interface, and 11067 to the active shallow crust. 1943 earthquakes remained unclassified, most of which were deep or $M_W < 5.0$. The classification results are presented in the Figure 4.

For more information on the tectonic classification algorithm, see the documentation at https://gemsciencetools.github.io/oq-mbtk/contents/sub.html.

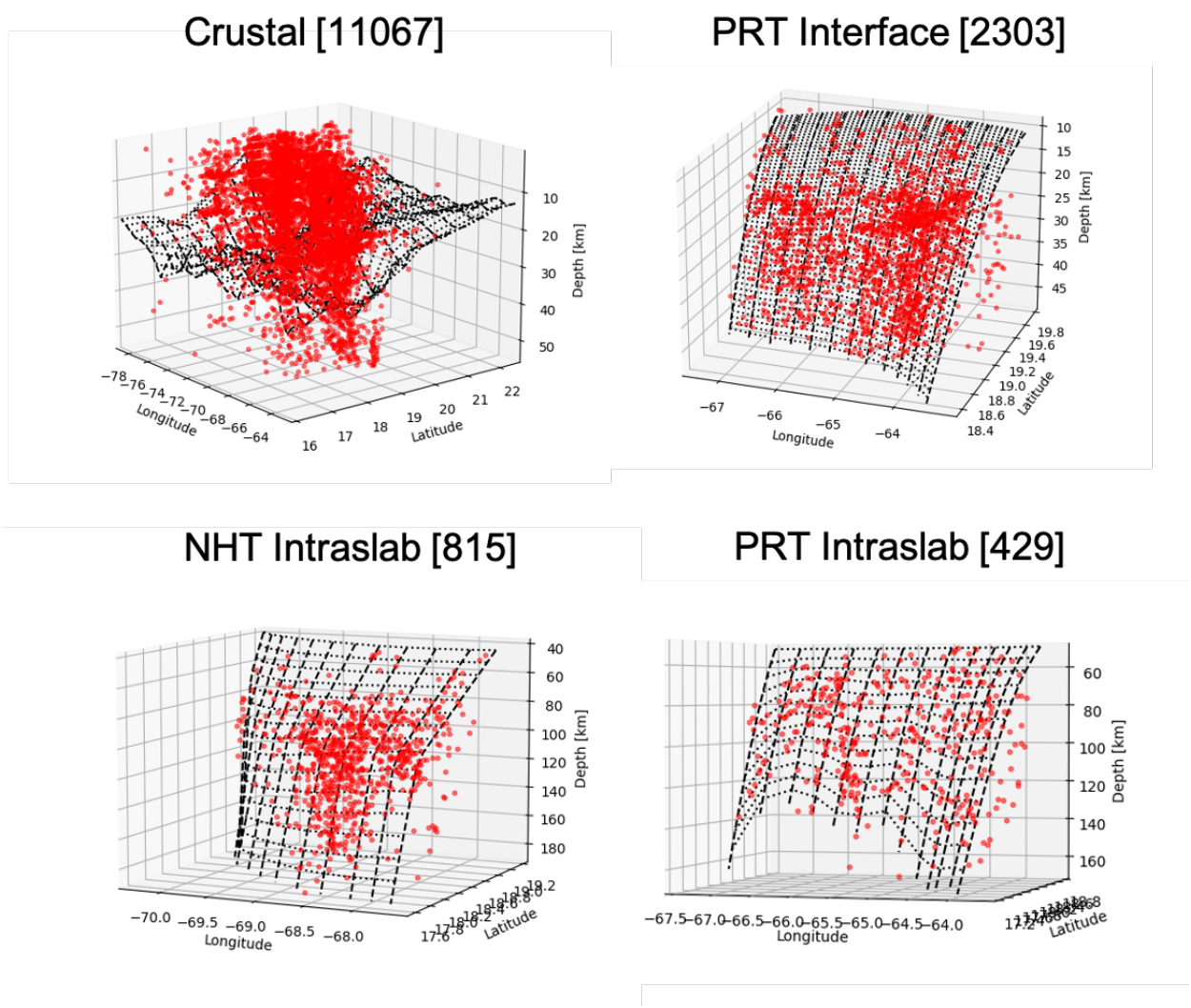

Figure 4 Surfaces used to classify the seismicity and the corresponding seismicity classified to the respective TRTs, with number of events listed in brackets. Top left: crustal seismicity (recall that this includes the LMT and NHT interfaces). Top right: PRT interface. Bottom left: NHT intraslab. Bottom right: PRT intraslab.

2.2 Active shallow fault database

In addition to the classified catalogue, the active shallow fault database is the most important dataset used to construct the DOM21 seismic source model. The active shallow fault database used herein, which was compiled in the context of the TREQ project, is based on two datasets: (1) the most recent CCARA fault database (updated from Styron et al., 2020), which is a part of GEM's Global Active Faults Database (GAF-DB; Styron and Pagani, 2020), and includes ~290 active shallow faults, and (2) an active faults database built by the SGN during the SYSMIN Program and Gran Santo Domingo projects (e.g., Bertil et al., 2015). In addition, for the characterization of some faults (fault kinematics and slip rates estimates) recent literature (i.e., Calais et al, 2016) and results from current SGN projects were used. We emphasize that the SGN contribution was critical to compiling a complete fault database for DOM21.

The final database used herein includes 84 fault traces from the CCARA database, which cover southeastern Cuba, Jamaica, Hispaniola, and Puerto Rico, and are both on and offshore (Figure 5). The faults offshore of Cuba – the Oriente Fault System and the Santiago deformed belt – were slightly modified (i.e., their segmentation) based on a more recent study by Rodriguez-Zurrunero et al., (2020). For all other cases, the parametrization used in the latest version of the Central America and Caribbean (CCA) model was maintained.

Then, we merged this set of faults with the national SGN compilation (e.g., Bertil et al., 2015). The first version of the SGN dataset contained 35 fault traces, and was further updated with data from a current SGN-IGME tectonic project dedicated to study the Septentrional fault (Yesica Perez, personal communication in the first phase of the TREQ project). The lastest version includes 40 fault traces located in Hispaniola (Figure 6).

The SGN faults were characterized following the standards proposed in Styron et al. (2020), and consistent with the approach to characterizing the faults coming from the CCA database. The geometric fault attributes are mostly provided by SGN (the exceptions are listed above), while kinematics (i.e. slip rates) were taken from either SGN compilations, or literature if they were not available in SGN studies/reports.

The compilation combining the two data sources initially contained 125 fault traces. Some major faults in the Hispaniola were duplicated, since they were mapped and characterized for both projects (see Figure 7). In general, the style of faulting and the parameters describing the geometry (dip, rake, dip direction) for these faults are quite similar, but differences were found on trace locations (including segmentation) and kinematics. The differences on trace locations can be associated to the mapping methods and the reference data. Since the trace locations are better constrained in the SGN database, these traces were used for all faults in Hispaniola, and the CCA traces were used for the rest of the study area. Kinematic disparities are more likely related to interpretation by the authors while constructing the databases, and on the data available at the time of study. Thus, our best judgement was used to select slip rates on a case-by-case basis.

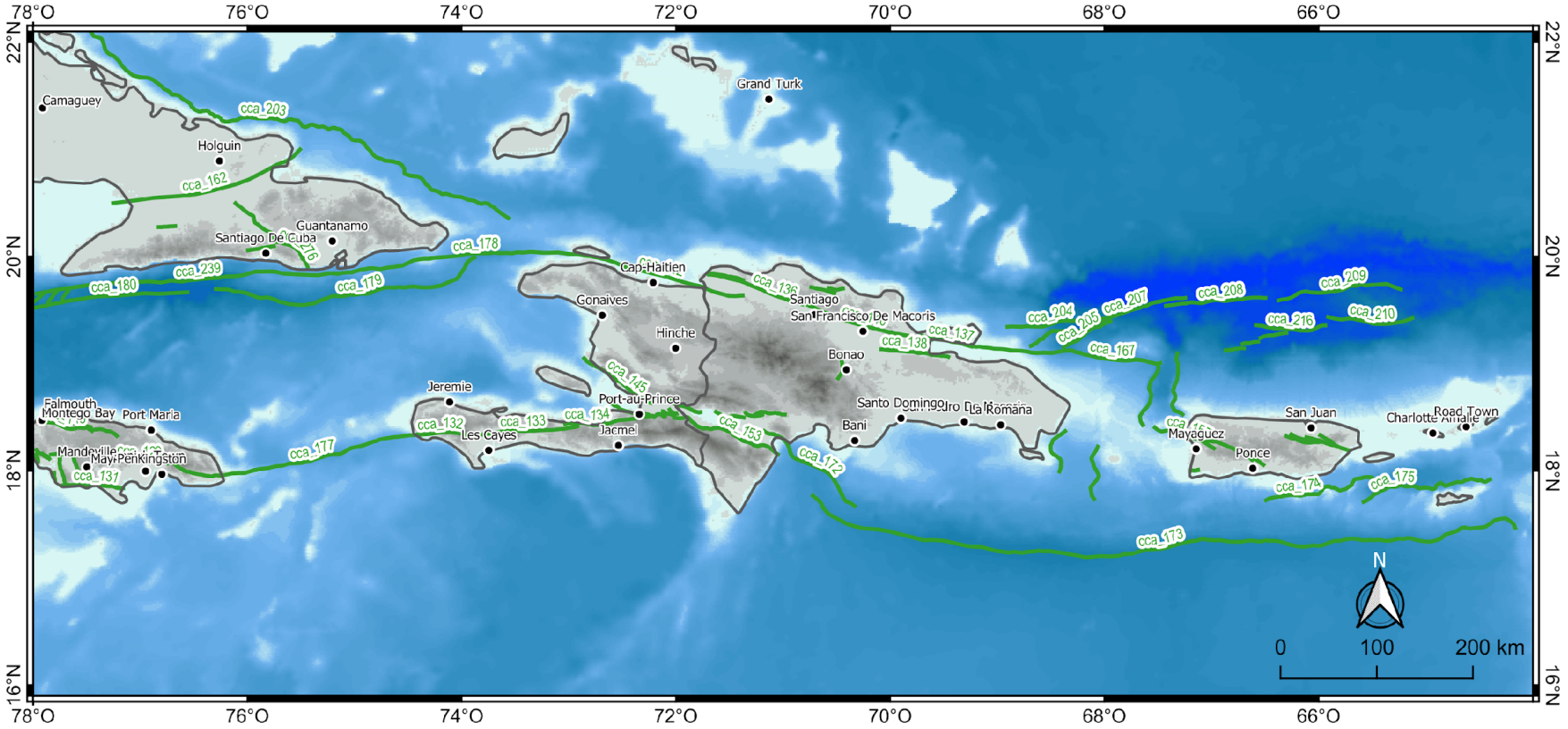

Figure 5. Faults sourced from the CCA database (updated from Styron et al., 2020). Fault IDs correspond to those in Table 6.

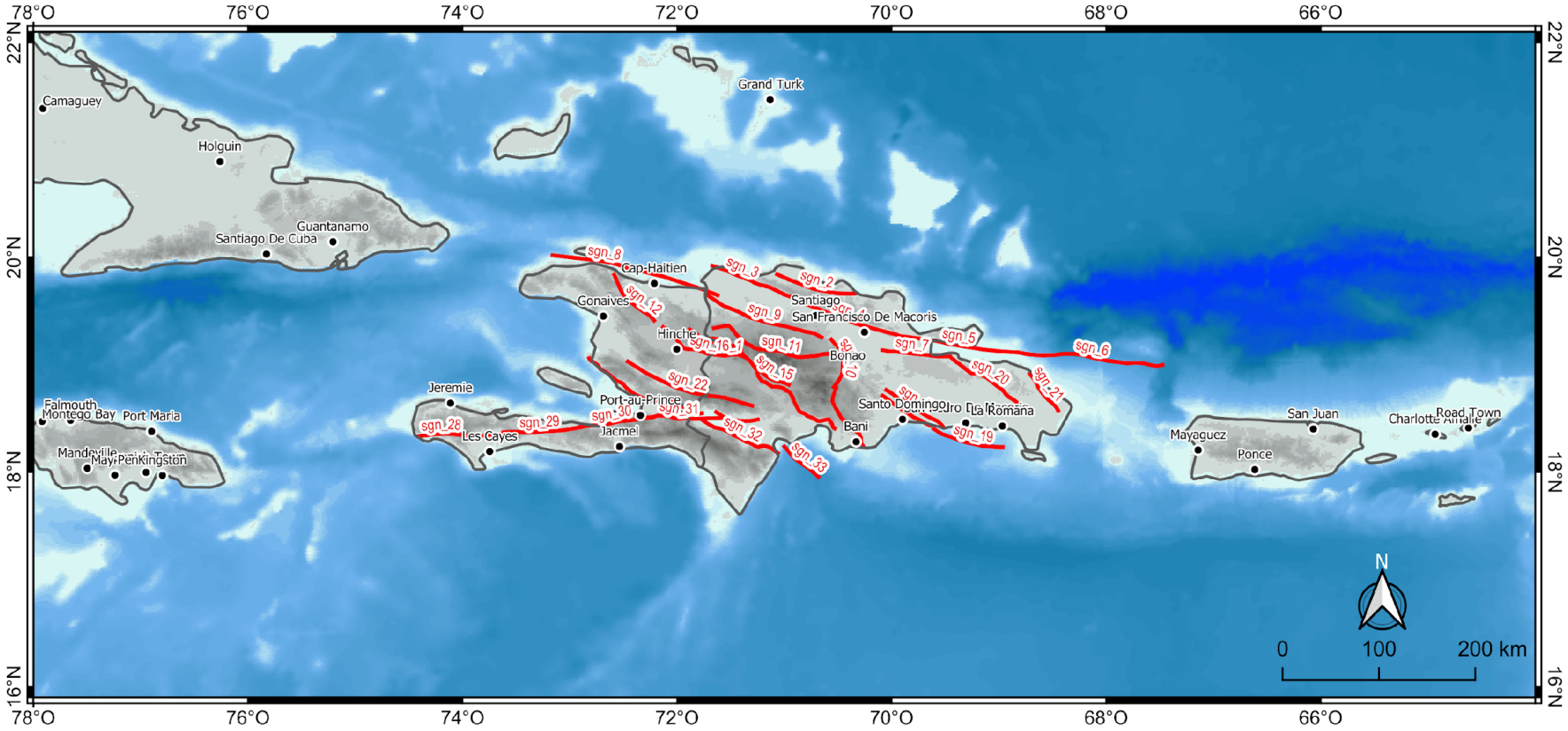

Figure 6 Faults contributed by the SGN database (e.g. Bertil et al., 2015). Fault IDs correspond to those in Table 6.

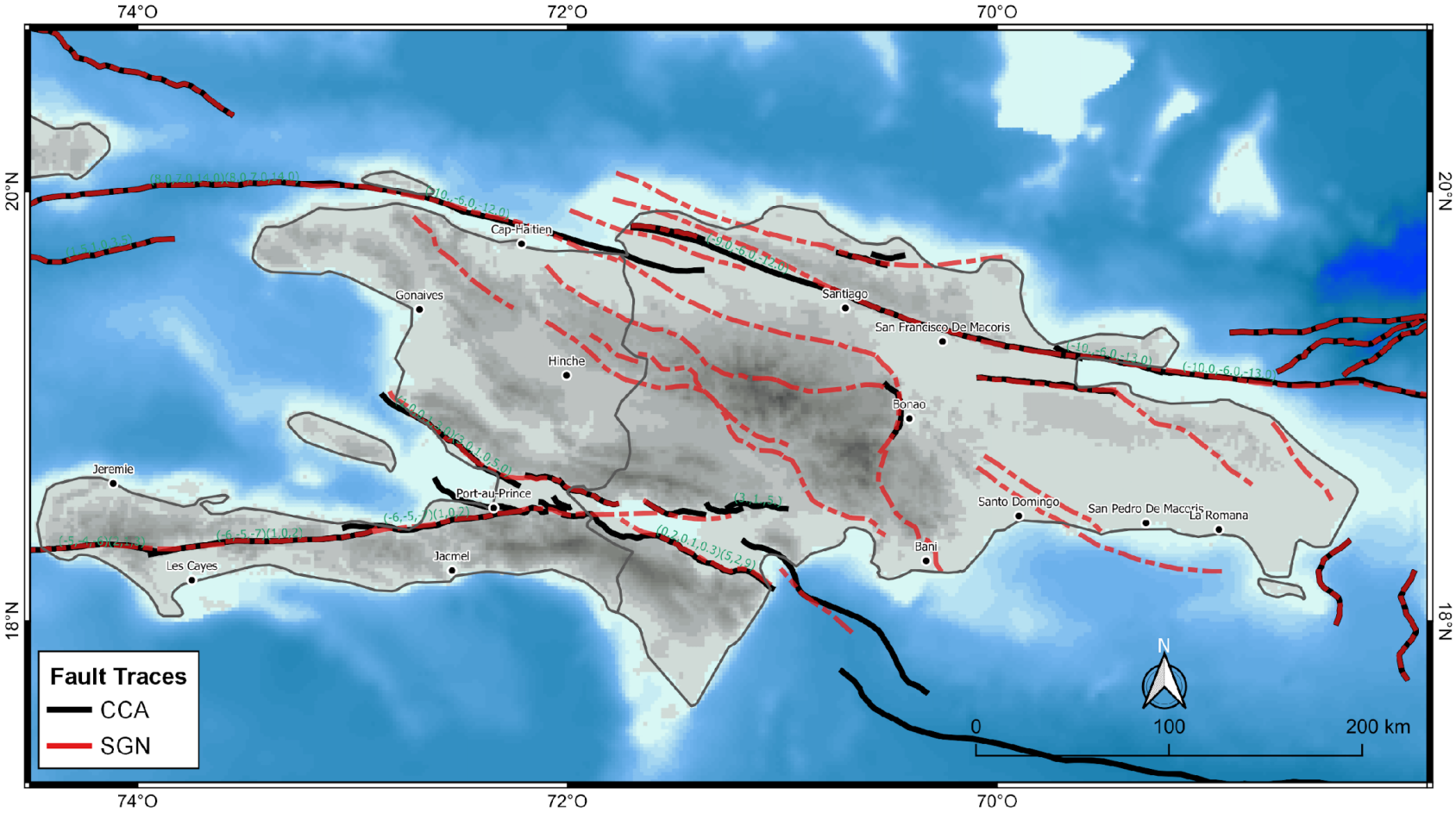

Figure 7 Fault traces in the compilation used in this study in close proximity to Hispaniola: 84 traces (black lines) come from CCA model and the rest (40 red dashed lines) from SGN compilations.

3 SEISMIC SOURCE CHARACTERIZATION

The seismic source characterization (SSC) for the DOM21 model includes multiple seismic source models that together represent all of the earthquakes that have been observed or are thought to be possible in and near Hispaniola, and accounting for some of their epistemic and aleatory uncertainties. Here, we discuss the source models in three groups that correspond to the primary tectonic domains defined in Section 2: (1) the PRT interface, (2) the intraslab sources, and (3) the collection of sources representing earthquakes in the active shallow crust and the NHT and LMT interfaces. For each group, we explain the chosen source typologies, and how the source geometries and occurrence properties are determined. Then, we describe the uncertainties that we incorporated into the SSC.

The SSC was carried out using a number of tools developed or maintained by GEM. In particular, we used the OQ-MTBK to model distributed seismicity and subduction sources, and the Seismic Hazard and Earthquake Rate In Fault Systems (SHERIFS) software (e.g. Chartier et al., 2019) to model ruptures occurring on the active shallow faults and the NHT and LMT interfaces. These tools are described within their respective sections.

3.1 Puerto Rico Trench interface

The Puerto Rico Trench (PRT) interface was characterized as an OpenQuake complex fault source, i.e., a 3D surface defined by a set of along-strike "edges" that are approximately equally spaced along the dipping interface surface. The edges are derived from the Slab 2.0 (Hayes et al., 2018) Puerto Rico Trench geometry and correspond to the same surface used to classify seismicity (Figure 4).

To determine the magnitude frequency distribution for the PRT interface, we explored MFDs based on (1) the observed seismicity classified to the interface in Section 2; (2) the fault dimensions and slip rate; and (3) using a combination of both factors. For (1) and (3), the classified observed seismicity was first declustered using the method by Gardner and Knopoff (1974) using the time and spatial windows by Uhrhammer (1986), and only the identified aftershocks were used to compute the seismicity-based MFDs; additionally, the catalogue was clipped to include only the seismicity within the defined magnitude-time completeness thresholds (Figure 9 caption).

In (1), the final subcatalogue was used with the Weichert (1980) method to derive a Gutenberg-Richter (GR) MFD with a-value = 4.74 and b-value = 1.00. M_{max} for (1) was derived by adding a delta of 0.3 to the magnitude of the largest observed earthquake (M_W 7.7 that occurred in 1943). For (2) we explored Youngs and Coppersmith (1985; YC) MFDs derived from slip-rates scaled by a coupling coefficient, using multiple M_{max} (M_W 7.9 – 8.2), coupling coefficients (0.08 – 1.0), and slip-rate (7.2 – 6.5 mm/yr) values from the literature (Symithe et al, 2015; Manaker, 2008; Terrier-Sedan & Bertil, 2021). In (3), we used the subcatalogue the same parameter ranges with the methodology from Pagani et al. (2020a) to create hybrid-type MFDs that decouple the processes controlling the "characteristic" magnitude earthquakes from the smaller magnitudes that occur according to a GR (see also Peñaruba et al., 2020; Johnson et al., 2021).

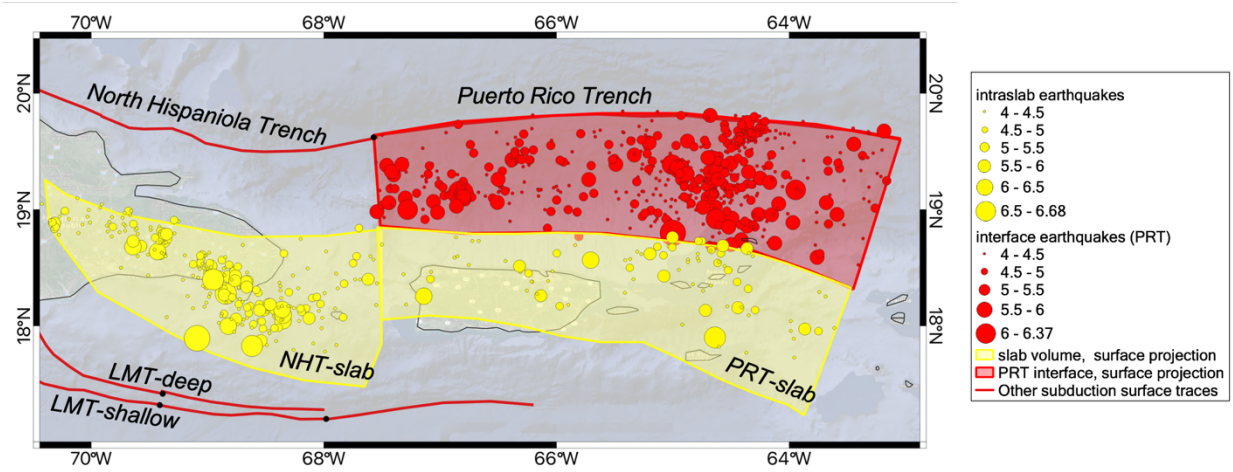

Figure 8 Subduction interface and subduction slab sources. The red lines show the surface projection of the top edge of faults classified as subduction interface in the proximity of the surfaces used for tectonic classification of seismicity (see Figure 4): the North Hispaniola Trench (NHT; NB this extends to the west), Puerto Rico Trench (PRT), and Los Muertos Trench (LMT). The red polygon shows the extent of the PRT interface, and the red circles are earthquakes MW>4.0 occurring since 1960 classified to this TRT. The yellow polygon and circles are the same, but for the intraslab TRT, separated into the NHT and the PRT. The black dots show where segments of the faults occur.

Considering the proximity of the PRT interface to Hispaniola (>100 km to the closest onshore sites), the rates of larger magnitude events have a much greater impact on the seismic hazard. Thus, we choose only two MFDs from the range of candidates: one GR MFD, which has lower rates of M>7 earthquakes, and one YC MFD. Both MFDs are supported by the observations – although we note that the rates of the highest magnitude occurrences may be biased by time-magnitude completeness – and represent endmember solutions (Figure 9). The two alternatives are equally weighted in the source model logic tree.

3.2 Intraslab sources

Both slabs were modelled using OQ Engine nonparametric sources (i.e., predefined ruptures with corresponding probabilities that are generated in advance of the hazard calculations) according to the method by Pagani et al. (2020a). The method takes the following steps: (1) for each slab volume, the classified, declustered subcatalogue for the respective slab or slab segment is used to derive a GR MFD using the Weichert (1980) method; (2) generate gridded ruptures within the slab volume, which is based on the slab-top surface geometry used to classify the seismicity; and (3) distribute the MFD rates across the gridded ruptures. In Pagani et al. (2020a), step (3) assigns a uniform rate to each rupture. Here, we built upon the original method to include a Gaussian-based smoothing kernel that distributes a portion of the occurrence rates according to past seismicity.

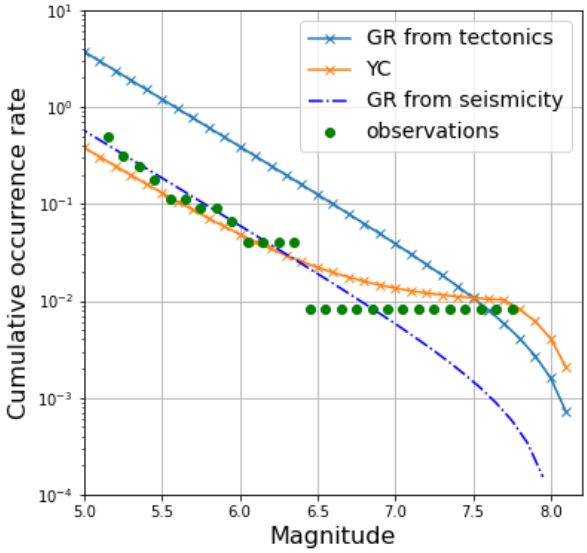

Figure 9 MFDs for the PRT interface. The green dots show the cumulative occurrence rates of observations (e.g. recorded earthquakes), while each line shows a tested MFD. The light blue line with crosses is the GR MFD computed from tectonics; dark blue is the GR MFD fit to the earthquake observations, and the orange line is the Youngs and Coppersmith (1985; YC) MFD from tectonics. All computed MFDs use b=1.0 (see text) and the completeness thresholds of [[2010, 5.0], [2000, 5.2], [1980., 5.5], [1960., 6.0], [1900., 7.0]].

The seismic source model for the Dominican Republic includes two intraslab sources: the downgoing slab of the North Hispaniola and Puerto Rico Trenches. The GR MFDs generated from the respective subcatalogues are listed in Table 4, with M_{min} = 5.5 and M_{max} = $M_{max,obs}$ + 0.3, but with a minimum of M_{max} = 7.0 (i.e. see the PRT MFD). For both slab sources, the surfaces used to classify the seismicity (see Figure 4) are also used to define the slab volumes within which the ruptures are produced; the surface is used as the top of the slab volume. The ruptures are generated on surfaces that dip at 45° and 135° respective to the slab top and extending for 60 km, using the magnitude scaling relationship for inslab seismicity by Strasser (2010) and rupture aspect ratios ranging from 2.0 – 8.0 to determine the rupture dimensions.

Two versions of the intraslab sources were included in the logic tree. In the first, 10% of the occurrences are distributed uniformly throughout the slab volume, while the other 90% is distributed using the smoothing kernel. In the second, the ratio is switched such that 90% of the seismicity is distributed uniformly. In the logic tree, the former model has a higher weight (0.7) based on our higher confidence in the model that assumes future inslab earthquakes are more likely to occur close to past earthquakes.

Table 4. Parameters of the GR MFDs computed for the intraslab TRT of the North Hispaniola Trench (NHT) and Puerto Rico Trench (PRT).

Intraslab Segment	*a*-value	*b*-value	M_{max}	$M_{max,obs}$	*Completeness [[year, M], ...]*
NHT	4.566	0.968	7.5	7.2	[[2000, 5.0], [1980, 5.5], [1960, 6.0], [1900.0, 7.0,]]
PRT	4.898	1.087	7.0	6.1	[[2000, 5.0], [1980, 5.5], [1960, 6.0], [1900.0, 7.0,]]

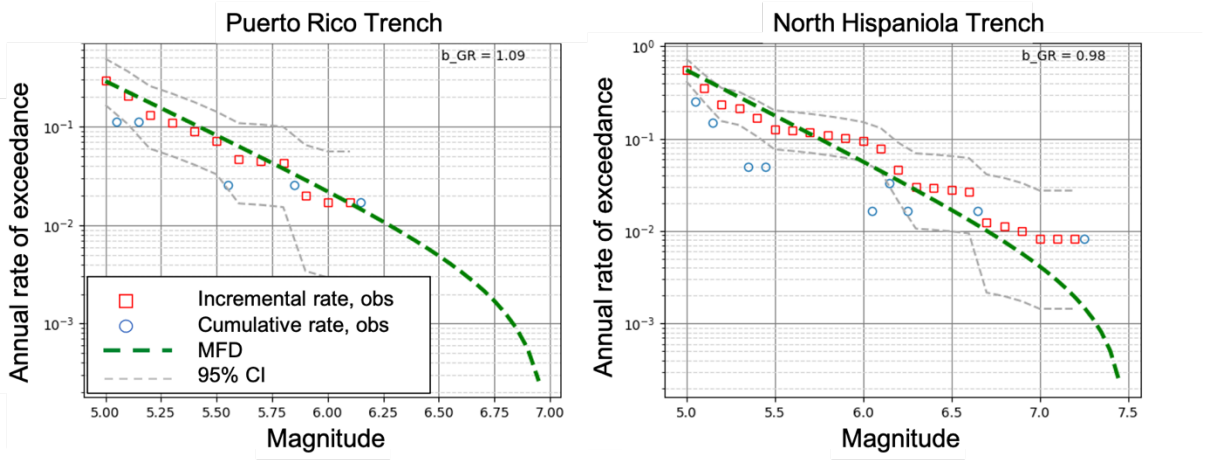

Figure 10 MFDs for the intraslab tectonic regions. Left: Puerto Rico Trench and Right: North Hispaniola Trench. The dashed green line shows the MFD fit to the observations, the blue circles show the incremental occurrence rates of earthquakes categorized to the respective slab, red squares show the cumulate occurrence rates for the same, and the dashed grey lines show the 95% confidence interval.

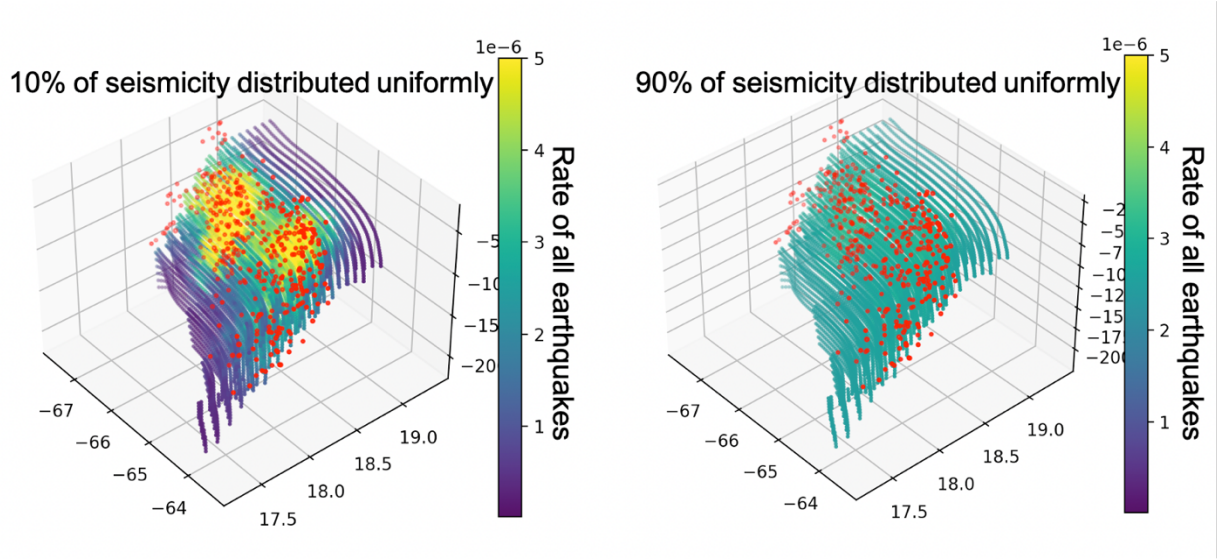

Figure 11 Example for the Puerto Rico Trench, where the modelled intraslab seismicity rates are smoothed (left) 10% uniformly and 90% according to the kernel, and (right) 90% uniformly and 10% according to the kernel. Each point represents a rupture hypocenter, and colored by the cumulative rate of all earthquakes assigned to that rupture.

3.3 Shallow crustal sources and NHT and LMT interfaces

The shallow crustal component of the source model is made up of two main parts: (1) distributed seismicity modelled by smoothing the occurrence rates of point sources across source zones, and (2) single- and multi-fault ruptures that capture the range of possible earthquake ruptures that could occur within the fault systems affecting Hispaniola. These sources are based on the subcatalogue classified to the shallow crust, the fault database, and the LMT and NHT interfaces as characterized by Terrier-Sedan and Bertil (2021).

The shallow crustal seismicity was characterized using the following steps:

(1) Define crustal source zones that will be used to create distributed seismicity sources
(2) Using the OQ-MBTK, characterize the geometry and occurrence properties of each source zone
(3) Apply smoothing kernels to distribute the modelled seismicity rates within a source zone across point sources according to positions of past earthquakes
(4) Using SHERIFS, create a rupture model that expends the slip rates of all faults in the fault database using single- and multi-fault ruptures
(5) Use SHERIFS and the OQ-MBTK to control the portion of the total modelled moment rate assigned to distributed seismicity versus the rupture model
(6) Repeat Steps 2-5 to incorporate epistemic uncertainties

In step (1), we defined a set of seven "source zones", i.e., areas (defined by a perimeter) with internally consistent tectonic and seismic characteristics, summarized in Table 5. The source zones are based on geological and geophysical data including plate boundaries, slip rate and sense of motion of crustal faults, and seismicity spatial patterns, but do not necessarily have spatially consistent rates. Then in Step (2), we characterized each source zone, assigning the following parameters: GR MFD; focal mechanism distribution; depth distribution and seismogenic depth limits; magnitude scaling relationship; and rupture aspect ratio. The MFDs and depth distribution parameters were derived from the declustered crustal subcatalogue clipped to the source zone and filtered for completeness. The MFDs use a fixed value of M_{min} = 5.0, while M_{max} is the magnitude of the largest observed earthquake in the source zone + 0.5.

In step (3), a Gaussian smoothing kernel is used to redistribute the total moment in each source zone onto a set of point sources that are located using level 4 of H3: Uber's Hexagonal Hierarchical Spatial Index[4]. At each grid point, the smoothing method, which is similar to that of Frankel (1995), takes into consideration each earthquake within a given distance, and uses the Gaussian kernel to determine how much more moment that grid point will produce in the source model relative to the other grid points. The kernel uses three Gaussians with standard deviations 20, 40, and 60 km weighted at 80%, 15%, and 5%, respectively and a maximum distance (radius) of 120 km. Traditionally when using this methodology, each earthquake has been given an equal weight when their impact is scaled using the smoothing kernel (i.e., in other GEM models such as Peñarubia et al., 2020, and Johnson et al., 2020). Here, we explored a second method of weighting the earthquakes, in which weights are based on the inverse of the completeness duration applied to the respective magnitude of the earthquake, which results in higher weighting for smaller magnitude earthquakes. This is defensible because then the smaller earthquakes – those which are expected to have higher rates in a relative sense, since all the MFDs use a Gutenberg-Richter negative-exponential MFD shape – are given more priority in the weighting schematic.

[4] https://github.com/uber/h3

Table 5 Description of the source zones (SZ) used to model crustal seismicity. a and b are the GR a- and b-values, Mmax is the maximum magnitude observed (obs) and modelled (mod), FM is the focal mechanism distribution given by strike/dip/rake and weight w, DD is the depth distribution pairs weight w, depth (km), and C is the completeness thresholds used in terms of year and magnitude.

SZ	description	*a*	*b*	M_{max} (obs/mod)	FM (strike/dip/rake, *w*)	DD (*w*, depth)	C (year, *Mw*)
1	Thrust faulting that marks convergence between the NA and C plates. Main structures: NHT and PRT. Seismicity rates on the NHT are high in the central and east, but sparser to the west	4.29	0.98	6.8/ 7.1	0/90/-90, 1.0	0.17, 5.0 0.31, 15.0 0.39, 27.5 0.13, 42.5	2000, 5.0 1980, 5.5 1960, 6.0 1920, 6.5 1900, 7.0
2	Shear zone that accommodates the sinistral component of NA-C convergence. Includes the Septentrionale and Oriente fault zones, which mostly trend ~E-W.	3.46	0.72	7.76/ 8.06	90/30/90, 0.64 90/90/0, 0.22 90/45/-90, 0.14	0.2, 5.0 0.4, 15.0 0.32, 27.5 0.08, 42.5	2000, 5.0 1980, 5.5 1960, 6.0 1900, 7.0
3	Sparse seismicity in the NA plate	3.15	0.80	6.87/ 7.17	0/90/-90, 1.0	0.16, 5.0 0.24, 15.0 0.55, 27.5 0.05, 42.5	2000, 5.0 1980, 5.5 1960, 6.0 1900, 7.0
4	Sparse seismicity in the Caribbean plate; transpression to the east and compression to the west	5.90	1.29	6.69/ 6.99	0/90/-90, 1.0	0.14, 5.0 0.26, 15.0 0.49, 27.5 0.11, 42.5	2000, 5.2 1980, 5.5 1960, 6.0 1940, 6.5 1900, 7.0
5	Includes most of the Gonave block, and the terrain-bounding Enriquillo-Plantain Garden fault zone. Faulting is predominantly E-W and sinistral/transpressive	3.73	0.86	7.80/ 8.10	100/45/90, 0.8 30/90/0, 0.2	0.22, 5.0 0.42, 15.0 0.29, 27.5 0.07, 42.5	2010, 4.6 2000, 5.0 1980, 5.5 1960, 6.0 1900, 7.0
6	The eastern peninsula, marked by mostly extensional faulting that overlies the Muertos thrust.	4.80	1.06	7.50/ 7.80	100/60/-90, 0.46 100/30/90, 0.54	0.26, 5.0 0.3, 15.0 0.38, 27.5 0.06, 42.5	2000, 5.0 1980, 5.5 1960, 6.0 1900, 7.0
7	Convergence zone between the NA and C plates. In the east the main structure is the E-W trending LMT. Further west the structures rotate toward WNW-ESE and include the Peralta belt front thrust, the Montagnes Noires fault, and the Matheux fault.	4.57	0.94	7.50/ 7.80	330/45/90, 0.64 210/90/0, 0.24 30/30/-90, 0.12	0.17, 5.0 0.31, 15.0 0.43, 27.5 0.09, 42.5	2010, 4.7 2000, 5.3 1980, 5.5 1960, 6.0 1900, 7.0

At the end of Step (3), the point sources for each source zone are divided into two sets that depend on their magnitude ranges. This is done by duplicating the point sources, and assigning each set one part of the MFD for each source. The first set accounts for magnitudes $M_W < 6.0$, while the second accounts for $M_W \geq 6.0$. This structure is used later in the workflow (Step 5), when the active shallow crustal point sources must be combined with the fault sources.

Step (4) characterizes the fault sources, using the Seismic Hazard and Earthquake Rates In Fault Systems (SHERIFS; Chartier et al., 2019) program to create ruptures on each fault in the database provided by SGN. SHERIFS is an open-source Python tool that considers individual faults together as a fault system, modelling annual rupture rates for ruptures permissible by the fault system, including those that are complex and multi-fault. The tool takes fault geometries and slip-rates as inputs, as well as hypotheses (made by the modeler) of the MFD shape for the total fault system. The faults, using their surface traces, dips, and dip directions, are cut into segments represented by OpenQuake kite surfaces, and fault slip-rates are divided among the segments based on their respective areas. Then, the segments are used to construct two types of sources - kite faults and non-parametric ruptures - that together satisfy the target MFD as defined by the fault area, slip-rates, and user-defined target MFD shape. The present model uses the following data and assumptions:

- Fault data: Fault traces, slip rates, sense of motion, dips, and dip directions as defined by the database compiled herein (see Section 2.2); described more explicitly in Table 6.
- Initial MFD: Gutenberg-Richter with *b*-value = 0.95 (an approximate average from the zones including faults)
- Magnitude scaling relationships and on-to-off fault seismicity (Table 7).

The fault sources are divisible into two categories. The first is single-section sources (kite faults), which produce ruptures ranging from M_W 6.0 – $M_{max,segment,}$ where $M_{max,segment}$ is the magnitude of an earthquake that would rupture the full segment; these are "typical" parametric sources in that they are evaluated by floating ruptures across the kite surfaces. The second type is multi-section ruptures, which accommodate the magnitudes that exceed $M_{max,segment}$. Each non-parametric rupture is assigned a corresponding annual probability of occurrence.

In addition to the faults in the database, the NHT and LMT interfaces are modelled using SHERIFS. This way, the variable along-strike slip rates on these interfaces can be used, while still permitting ruptures to connect segments of the faults that slip at different rates. Additionally, these interfaces are poorly constrained relative to the PRT, having infrequent seismicity that distinguishes a zone more-so than a surface; thus, their occurrence rates cannot be constrained using only earthquake observations, and the faults themselves should be balanced with the off-fault seismicity modelled in Step (3). However, we did not permit ruptures to connect these interface surfaces to the crustal faults.

Step (5) combines the sources and ruptures constructed in Steps (3) and (4) to produce a single crustal source model that does not "double-count" any of the modelled seismicity. This is done within SHERIFS using ad-hoc adaptations to the code. The point sources from Step (3) with $M_W \geq 6.0$ are clipped to a polygon that bounds the faults plus a buffer (shown in Figure 12), indicating the points across which the sources must be balanced. Additionally, a magnitude-dependent on-fault to off-fault seismicity is provided within the SHERIFS. The ratios dictate the portion of the seismicity that is allotted to the kite

sources and ruptures versus the point sources; the rates or probabilities for each are scaled accordingly.

In Step (6), epistemic uncertainties are introduced to Steps (3) and (4) of the work flow using a logic tree where each uncertainty corresponds to one branch set. This was done by making multiple hypotheses or assumptions about the following uncertain parameters used to construct the active shallow crustal source model:

- Weighting approach used to smooth the distributed seismicity (2)
- Slip rate on the Orientale and Enriquillo-Plantain Garden strike-slip fault systems (3)
- Magnitude-scaling relationship used in SHERIFS (2)
- Ratio of on-fault to off-fault seismicity (2)

Smoothing approach: As mentioned for Step (3), we used two different approaches to weight the observed earthquakes when distributing the seismic moment across each source zone: uniform weighting of earthquakes, and magnitude-completeness based weighting, as shown in Figure 14. One noteworthy discrepancy between the two outcomes is that in the latter interpretation, more weight is given to recent observed earthquakes occurring near faults in the central part of Hispaniola near the border between Haiti and the Dominican Republic, a region with multiple faults according to the SGN database. The two smoothing approaches were weighted equally in the logic tree.

Fault slip rate: In an optimal case, the epistemic uncertainty included herein would account for the full range of possible slip rates for each fault in the SGN database. However, the faults in the SGN represent multiple fault systems in which the slip rates of all faults together accommodate the deformation occurring in the region; thus, it is not possible to change the slip rate of one fault without recomputing the slip rates for one or more other faults in the system. Thus, for the fault sources, we used a primary model with the 'preferred' slip rate for each fault segment (i.e. as indicated by SGN in the fault database), and two alternative models that in which the rates of the sinistral components of two significant structures are varied: to the north, the Oriente fault and the part of the Hispaniola fault with which it is still ~continuous along strike, and to the south, the Enriquillo-Plantain Garden fault and its along-strike structures for the longitudinal range covered by the northern structures. To the east of here, the system is too complex and more rate balancing would require thorough analysis.

Table 8 lists the structures involved, and the preferred, minimum, and maximum sinistral component of slip rate. The structures are grouped by sections in which there is longitudinal overlap. The primary model uses the preferred sinistral slip rate for the faults in all sections, following the same standard as all faults in the model. For the alternative models, the sinistral slip rate for each fault is adjusted toward the minimum or maximum limit, and then the opposite change in rate is applied to the corresponding faults. For example, when the northern structure slip rates increase, the southern structures slip rates decrease by the same amount. In most cases, the magnitude of the admitted range is not equal between the two systems, so instead the smaller delta value between "preferred" and "minimum" or "preferred" and "maximum" is used to define alternative rates. The one exception is for the Blue Mountain fault; the delta value of 0.5 mm/yr was ignored in choosing the delta value for that portion of the system.

Table 6 Faults for which ruptures were created using SHERIFS. dir is the direction the fault is dipping, and dip is the dip angle in degrees. slip_type is the sense of motion on the fault. lsd and usd are the lower and upper seismogenic depths, respectively, in km. v_rl and v_ex are the right/left lateral (negative is left) and extensional/compressional (negative is compressional) velocities modelled on the faults, derived by taking the corresponding components of the net slip-rate. The reference indicates the source of the fault information. BRGM refers to the BRGM project, DEV HISPALEA 2014-2015.

name	dip	dir	slip_type	lsd	usd	v_rl	v_ex	reference
NHT-E	25.4	S	Reverse	40	0	5	0	Terrier-Sedan and Bertil, 2021
NHT-W	30	S	Reverse	50	0	6	0	Terrier-Sedan and Bertil, 2021
NHT-W-End	45	S	Reverse	50	0	4.3	0	Terrier-Sedan and Bertil, 2021
LMT-Centre East-shallow	16.7	N	Reverse	6	0	4.6	0	Terrier-Sedan and Bertil, 2021
LMT-Centre West-shallow	16.7	N	Reverse	7	0	6.2	0	Terrier-Sedan and Bertil, 2021
LMT-E	31	N	Reverse	40	0	0.8	0	Terrier-Sedan and Bertil, 2021
Camus Fault W	70	N	Sinistral	20	0	1	0	SGN
Septentrional Fault W	70	N	Sinistral	20	0	-8	0	Calais et al. 2016
Hispaniola Fault 01	70	N	Sinistral	20	0	10	0	
San Juan-Restauracion Fault Zone 01	70	N	Reverse	20	0	1.1	0	Benford 2012; Calais et al., 2016
Peralta Front Thrust 01	70	N	Reverse-Sinistral	20	0	0.6	0	Benford 2012; Calais et al., 2016
San Juan-Restauracion Fault Zone 06	70	E	Reverse	20	0	1.8	2.5	
San Juan-Restauracion Fault Zone 03	70	N	Reverse	20	0	0.2	0	
San Juan-Restauracion Fault Zone 02	70	N	Reverse	20	0	0.2	0	
Bonao-La Guacara Fault Zone C	70	S	Reverse-Sinistral	20	0	0.4	0	SGN
Bonao Fault	70	W	Reverse	20	0	0.4	0	SGN, BRGM/RP-65305-FR 2015
Matheux Fault 01	70	N	Reverse	20	0	1	0	Pubellier et al., 2000 Tectonics; Benford 2012; Calais et al., 2016
Matheux Fault 02	70	N	Reverse	20	0	1	0	Pubellier et al., 2000 Tectonics; Benford 2012; Calais et al., 2016
Muertos-Punta Salinas Fault	70	N		20	0	0.2	0	BRGM, 2015
Bahoruco Fault Zone	70	S	Reverse	20	0	0.2	0	BRGM 2015

name	dip	dir	slip_type	lsd	usd	v_rl	v_ex	reference
Enriquillo Fault 04	70	S	Sinistral	20	0	-7	4	Benford et al., 2012, Calais et al., 2010, Calais et al., 2016
Hispaniola Fault 03	70	N	Sinistral	20	0	1	0	SGN
Septentrional Fault C	70	N	Sinistral	20	0	-10	0	Calais et al. 2016
Vacama Fault	70	E	Normal-Dextral	20	0	0.2	0	BRGM 2015
Rio Yabon Fault	70	W	Normal-Dextral	20	0	0.2	0	BRGM 2015
San Pedro Basin Fault	70	W	Normal	20	0	0.2	0	BRGM 2015
Espanola Fault-South	70	W	Normal-Dextral	20	0	0.1	0	BRGM 2015
Espanola Fault-North	70	W	Normal-Dextral	20	0	0.1	0	BRGM 2015
Septentrional Fault E	70	N	Sinistral	20	0	-10	0	Calais et al. 2016
Septentrional Fault End	70	N	Sinistral	20	0	-8	0	Calais et al. 2016
Enriquillo Fault 03	70	S	Sinistral	20	0	-7	4	Benford et al., 2012, Calais et al., 2010, Calais et al., 2016
Enriquillo Fault 01	70	S	Sinistral	20	0	-7	4	Benford et al., 2012, Calais et al., 2010, Calais et al., 2016
Enriquillo Fault 02	70	S	Sinistral	20	0	-7	4	Benford et al., 2012, Calais et al., 2010, Calais et al., 2016
San Juan-Restauracion Fault Zone 05	70	N	Reverse	20	0	0.2	0	
Neiba Fault	70	N	Reverse	20	0	1	0	Saint Fleur et al., 2015 GRL; Calais et al., 2016
Matheux Fault 03	70	N	Reverse	20	0	1	0	Pubellier et al., 2000 Tectonics; Benford 2012; Calais et al., 2016
Peralta Front Thrust 03	70	N	Reverse	20	0	0.6	0	Benford 2012; Calais et al., 2016
Peralta Front Thrust 04	70	N	Reverse	20	0	1.8	2.5	Benford 2012; Calais et al., 2016
Duanvale Fault	60	S	Sinistral-Reverse	20	0	0.5	0	Mann et al., 2007
Duanvale Fault East	60	S	Sinistral-Reverse	20	0	0.5	0	Mann et al., 2007
Rio Minho-Crawle River Fault	90	N	Sinistral	20	0	-5	1	Benford et al., 2015

name	dip	dir	slip_type	lsd	usd	v_rl	v_ex	reference
Cavaliers Fault	90	N	Sinistral	20	0	-5	0	Benford et al., 2015
Blue Mountain Fault	60	NE	Reverse	20	0	2	2.6	Benford et al., 2012; Benford et al., 2015; Dominguez Gonzalez et al., 2015; Draper2008
South Coast Fault	90	N	Sinistral	20	0	2	0	Benford et al., 2012; Benford et al., 2015
Enriquillo-Plantain Garden Fault	90	S	Sinistral	20	0	3.2	0	Benford 2012
Oriente Fault Este	90	N	Sinistral	20	0	8	0	Leroy et al., 2015 Terra Nova; Calais et al., 2016; Benford 2012
Santiago Deformed Belt W	70	N	Reverse	20	0	0	1.5	Benford 2012; Leroy et al., 2015 Terra Nova
Oriente Fault Oeste	90	N	Sinistral	20	0	6	0	Benford 2012, Leroy et al., 2015 Terra Nova
Plantain Garden Fault	90	N	Sinistral	20	0	5	0	Benford et al., 2015; Koehler et al., 2013
Baconao B	60	NE	Normal	20	0	0.05	0	Magaz et al., 1997
Baconao A	60	NE	Normal	20	0	0.05	0	Magaz et al., 1997
Boniato	65	S	Normal	20	0	0.1	0	Magaz et al.,1997
Cerro Goden Fault	80	S	Sinistral	20	0	1	0	Mann et al., 2005
Great Southern Puerto Rico Fault Zone	70		Sinistral	20	0	1	0	Mann et al., 2005
West Mona Rift Fault	60	E	Normal	20	0	0.2	-1.5	Benford 2012
East Mona Rift Fault	60	W	Normal	20	0	0.2	-1.5	Benford 2012
West Yuma Rift Fault	60	E	Normal	20	0	0.15	-1.5	Hippolyte et al., 2005 GSA SP, Benford 2012
East Yuma Rift Fault	60	W	Normal	20	0	0.15	-1.5	Hippolyte et al., 2005 GSA SP; Benford 2012
Anegada Rift	60	N	Normal	20	0	0	-0.5	Mann et al., 2005 GSA SP; Benford 2012
St. Croix Fault	60	N	Normal	20	0	0	-0.5	Mann et al., 2005 GSA SP; Benford 2012
Great Northern Puerto Rico Fault Zone	90	N	Sinistral	20	0	0.1	0	Jansma and Mattioli 2005
Great Northern Puerto Rico Fault Zone	90	N	Sinistral	20	0	0.1	0	Jansma and Mattioli 2005

name	dip	dir	slip_type	lsd	usd	v_rl	v_ex	reference
Great Northern Puerto Rico Fault Zone	90	N	Sinistral	20	0	0.1	0	Jansma and Mattioli 2005
Great Northern Puerto Rico Fault Zone	90	N	Sinistral	20	0	0.1	0	Jansma and Mattioli 2005
Camu Fault E	80	N	Sinistral	20	0	1	0	SGN
Villa Vazquez fault	80	S	Sinistral	20	0	1	0	SGN, personal communication
Monte Cristi Fault	80	N	Sinistral	20	0	1	0	CCA and SGN
Bonao-La Guacara Fault Zone E	45	S	Reverse-Sinistral	20	0	0.4	0	SGN
Bonao-La Guacara Fault Zone W	45	S	Reverse-Sinistral	20	0	0.4	0	SGN
Peralta Front Thrust 02	45	N	Reverse-Sinistral	20	0	0.6	0	Benford 2012; Calais et al., 2016
Hispaniola Fault 02	80	N	Sinistral	20	0	1	0	SGN
Santiago Deformed Belt E	70	N	Reverse	20	0	0	1.5	Benford 2012; Leroy et al., 2015 Terra Nova
Oriente Fault Centro	90	N	Sinistral	20	0	6	0	Benford 2012, Leroy et al., 2015 Terra Nova
LMT-Centre East-deep_1	34	N	Reverse	40	6	0.92	0	Terrier-Sedan and Bertil (2021)
LMT-Centre West-dep_7	30	N	Reverse	40	7	1.24	0	Terrier-Sedan and Bertil (2021)

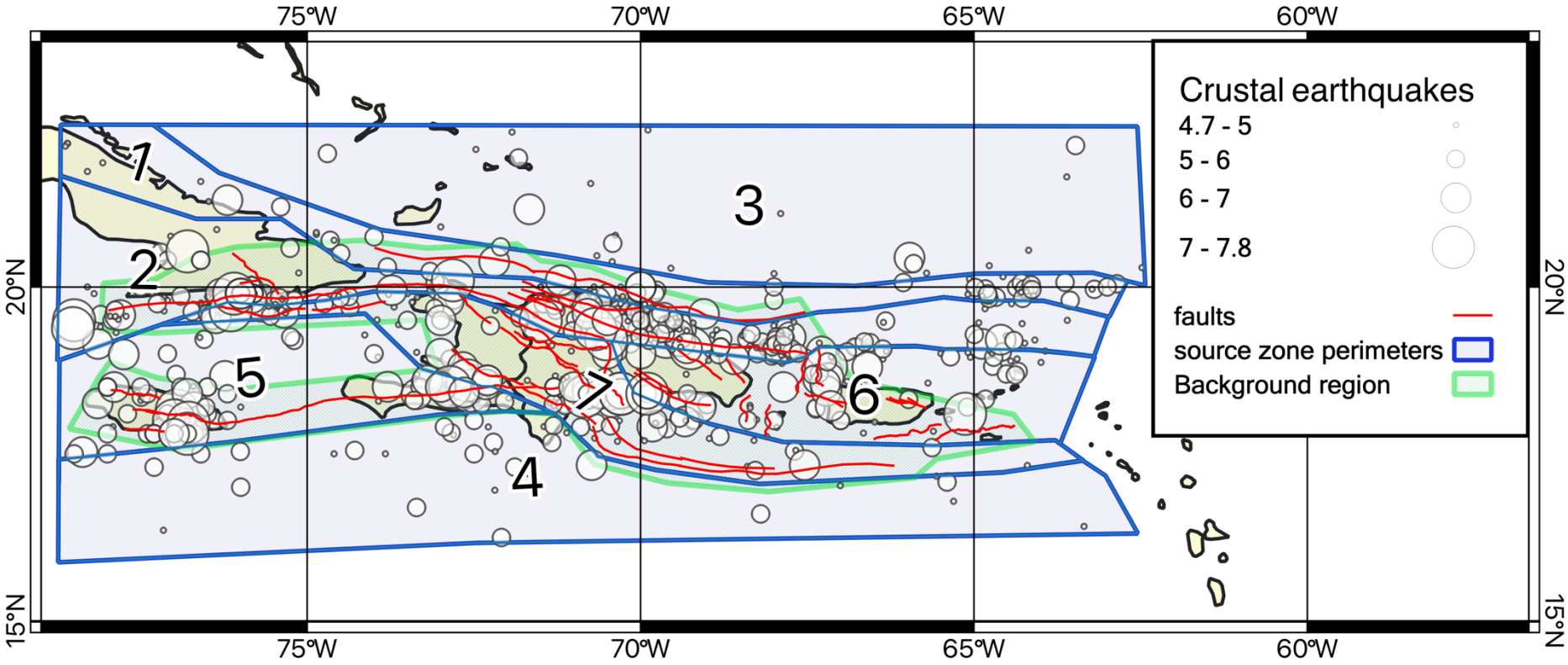

Figure 12 Source zones (blue; labeled to correspond with Table 5), faults modelled within SHERIFS (red), earthquakes classified as crustal (white circles) with MW >= 4.7, and clipping perimeter (green; see text).

Table 7 On-to-off-fault seismicity ratios. "Ratio" indicates the proportion of seismicity in the given magnitude range that is modelled on the faults.

Magnitude	Ratio 1	Ratio 2
6.0 – 6.5	0.8	0.7
6.5 – 7.0	0.9	0.8
7.0 – 7.5	1.0	0.9
7.5 – 8.0	1.0	1.0
8.0 - M_{max}	1.0	1.0

Table 8 Faults for which epistemic uncertainty in the sinistral component is considered. The listed preferred, minimum, and maximum sinistral slip rates are from the SGN database. The model 1, model 2, and model 3 sinistral slip rates correspond to the three considered models. Model 1 uses 'preferred' slip, model 2 puts more slip on the northern system, and model 3 puts more slip on the southern structures.

Northern Structures [name – (preferred, minimum, maximum) sinistral slip rate in mm/yr – section]	**Northern Structures** [(model 1, model 2, model 3) sinistral slip rate in mm/yr]	**Southern Structures** [name – (preferred, minimum, maximum) sinistral slip rate in mm/yr – section]	**Southern Structures** [(model 1, model 2, model 3) sinistral slip rate in mm/yr]
Oriente Fault Oeste – (6, 5, 14) – 1	(6, 8, 5)	Cavaliers Fault – (5, 3, 7) – 1	(5, 3, 6)
Oriente Fault Centro – (6, 5, 14) – 2	(6, 7.2, 5)	Blue Mountain Fault (2, 1, 2.5) – 1	(2, 1, 2.5)
Oriente Fault Este – (8, 7, 14) – 3	(8, 9, 7)	Plantain Garden Fault – (5, 3, 7) – 1	(5, 3, 6)
Hispaniola Fault 01 – (10, 8, 12) – 4	(10, 11, 9)	Enriquillo-Plantain Garden Fault – (3.2, 2, 5) – 2	(3.2, 2.0, 4.2)
		Enriquillo Fault 01 – (7, 6, 8) – 3	(7, 6, 8)
		Enriquillo Fault 02 – (7, 6, 8) – 3	(7, 6, 8)
		Enriquillo Fault 03 – (7, 6, 8) – 4	(7, 6, 8)
		Enriquillo Fault 04 – (7, 6, 8) – 4	(7, 6, 8)

Magnitude scaling relationship: We used two magnitude scaling relationships (MSRs) in SHERIFS to determine the magnitude attributable to each fault section and multi-fault rupture: the magnitude-area empirical relationships for Wells and Coppersmith (1994) and Leonard et al. (2010) (the intraplate relationship). The same MSRs are also used with the fault sources to produce ruptures. In addition to changing the rupture geometries, the MSRs also compute different values of M_{max} values for each

segment, modifying the MFD shapes, and therefore we do not additionally incorporate a formal M_{max} branch of the logic tree.

On-to-off-fault seismicity ratio: The occurrence rates of earthquake magnitudes modelled by fault sources and ruptures (M_W 6.0 and larger) must be adjusted such that the occurrences in the background seismicity are not "double-counting" any sources. This is done using magnitude-dependent on-to-off-fault seismicity ratios as in Step (5). Here, we use two sets of ratios, equally weighted in the logic tree, thus changing the amount of seismicity that was modelled by the faults versus in the distributed seismicity. This further modifies the MFDs used to define occurrences on the faults, as well as the surrounding distributed seismicity. The ratios are listed in Table 7. Both hypotheses model the majority of seismicity M_W > 6.0 on the faults, while Ratio 2 models attribute a small amount more to the distributed seismicity, allowing some earthquakes up to M_W 7.5 to occur in the distributed sources. A single ratio is used for the entire fault system, and so the alternative hypotheses impact the full spatial extent; this logic adds only two branches to the logic tree, rather than two branches per structure.

The final logic tree for the seismic source characterization that uses the distributed seismicity and SHERIFS workflow includes 24 branches. Figure 13 shows two examples how the logic tree manifests as MFDs for a single fault: the Muertos-Punta Salinas Fault which is just offshore of the southern coast of the Dominican Republic, and Segment 4 of the Peralta Front Thrust in the central part of the island. In both cases, the rate of M_W 6.0 earthquakes varies by an order of magnitude, and the M_{max} varies.

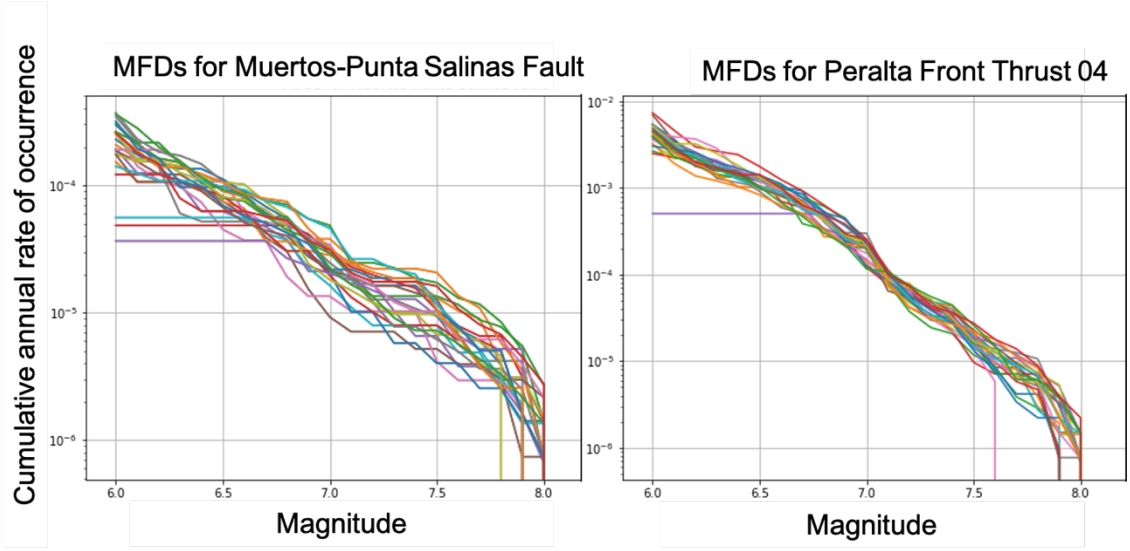

Figure 13 The 24 MFDs for (left) the Muertos-Punta Salina Fault and (right) the Peralta Front Thrust, segment 04.

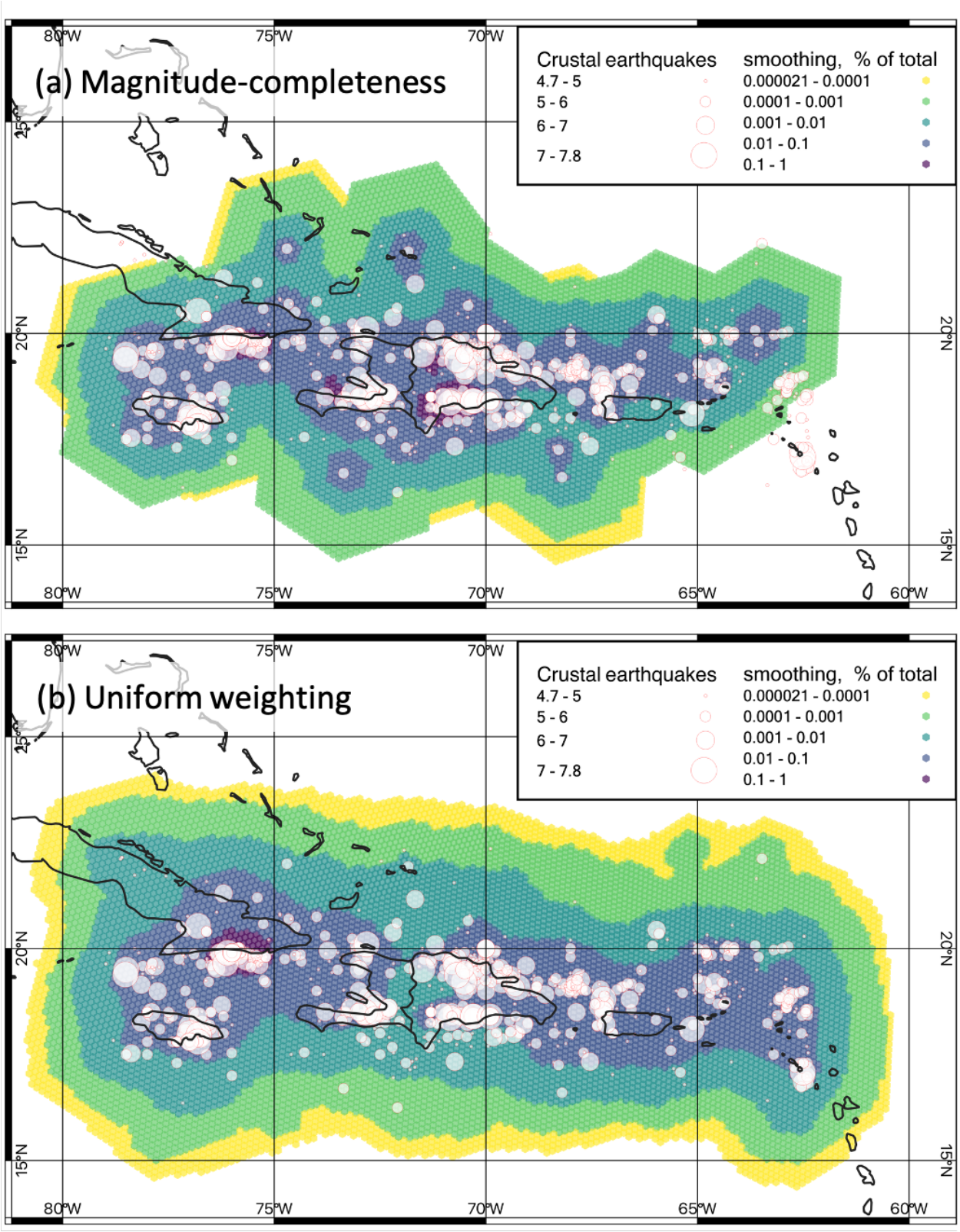

Figure 14 Smoothing approaches, depicting the weight applied spatially to the occurrence rates of point sources (i.e. not the final occurrence rates). (a) Magnitude-completeness. (b) Standard, uniform weighting per earthquake

3.4 Source model validation and tests

The seismic source model should be validated by applying basic sanity checks, and confirming that the model is capable of producing the earthquake observations used to construct the model. Here, we do this using GEM's tool "Hamlet" to evaluate how the seismicity produced by the model compares to the original catalogue, assessing the independent tectonic region types of the model and the different realizations (i.e., each end branch of the logic tree).

The Hazard Model Evaluation and Testing (Hamlet) is a Python tool that facilitates qualitative and quantitative tests to evaluate seismic source models developed for PSHA. At present, Hamlet's predominant approaches retrospectively test the earthquake occurrence models of the SSC against the earthquake catalogue used in preparing the SSC, or prospectively against more recent records or other data not used to develop the model. These tests include likelihood-based approaches, such as those by the Regional Earthquake Likelihood Models (RELM) and Collaboratory for the Study of Earthquake Predictability (CSEP; e.g., Schorlemmer et al., 2007, 2010; Zechar et al., 2010), as well as similar methods developed by GEM alongside Hamlet, and standard sanity checks such as comparisons of the model M_{max} to the observed M_{max}.

Here, we use Hamlet's implementation of the following tests:

- **Maximum magnitude check:** confirms that all spatial bins produce earthquakes with magnitudes at least as large than what has been observed
- **N-test** (modified version of Zechar et al., 2010): checks if the total number of observed events with $M > M_{min}$ (a lower magnitude threshold for testing – not necessarily of the model itself) is within a range given by a specified percentile of the Poisson distribution (the forecasted number of events is the mean of the distribution). Spatial and additional magnitude information are ignored.
- **M-test** (Zechar et al., 2010): compares MFDs from the catalogue of observed earthquakes used to produce the model to MFDs of stochastic event sets with an equal length to the catalogue generated sampling the source model. The model "passes" the test if the likelihood score of the model to the observations exceeds the likelihood of some critical percentile of the simulations.
- **S-test** (Zechar et al., 2010): equivalent to the M-test, but testing relative frequencies of observed vs modeled earthquakes using spatial bins that cover the model domain.

Hamlet works by generating all the ruptures that the source model permits, and simulates event sets based on these ruptures, grouping them into magnitude and spatial bins (Note: the spatial discretization use the same H3 cells used by the OQ-MBTK to produce the active shallow crustal distributed seismicity sources). The catalogue observations are binned in the same manner, and then the tests are executed in order to compare the two sets. For more information on the testing details, see Zechar et al. (2010) and the supplement of Johnson et al. (2020).

For all tests, we use a single catalogue that combines all the tectonic regions, combining the declustered versions of each into a single catalogue. The catalogue was truncated to a 40-year period starting in 1980, which corresponds to a completeness of M_W 5.5: the lower magnitude bound on the

subduction intraslab sources (the other TRTs extend to lower magnitudes) and thus a reasonable M_{min} to use for the Hamlet tests.

Here, we independently tested each of the 96 end branches of the source model, and used the following configuration parameters throughout:

- **Magnitude range:** M_W 5.5 – 8.5, binned by 0.2
- **Investigation time (all tests):** 40 years
- **N-test confidence interval:** 95%
- **M-test critical percentile:** 0.25
- **S-test critical percentile:** 0.25
- **Number of iterations (all tests):** 1000

All 96 end branches pass the maximum magnitude, N-test, and S-test, while 87 pass the M-test. The nine end branches that do not pass the M-test are very close to the critical percentile (i.e., higher than 0.237); given that the original authors (Zechar et al., 2010) proposed a threshold of 0.025, we consider the M-test results of these nine end branches to still show strong model performance.

4 Ground Motion Characterization

The ground motion characterization (GMC) for the DOM21 model initially adopted the GMC developed in the CCARA project (the Caribbean and Central America model, CCA). This was defensible because:

- The CCA model coverage includes the Dominican Republic and its three tectonic region types (active shallow crustal, subduction interface, and subduction intraslab).
- The CCA GMPE selection was performed using data from the Lesser Antilles and El Salvador. Like the Lesser Antilles, high attenuation has been observed in Haiti and greater Hispaniola (e.g., Castro et al., 2003; McNamara et al., 2012).
- Insufficient new strong motion recordings were available to merit repeating the analysis.

In CCARA, the GMC was performed by a GMPE selection process that uses the OpenQuake Strong Motion Toolkit (Weatherill, 2014). The three main steps were:

1) Preselection of a set of candidate GMPEs for each tectonic environment considered (e.g., Bommer et al., 2010; Cotton et al., 2006);
2) Comparative scaling of the pre-selected GMPEs using a suite of rupture scenarios with a range of magnitudes and source-to-site distances for several ground motion parameters (i.e., the trellis plot approach); and
3) Residual analysis to compare the ground motions computed by the pre-selected GMPEs and the ground motions observed (i.e. peak values from strong motion recordings in the Lesser Antilles and El Salvador) in the study area (e.g. Scherbaum et al., 2004).

In the final selection, a set of GMPEs (rather than a single one) was chosen for each region. This was due in part to the notable observed difference in attenuation for intra-slab earthquakes in the Lesser Antilles versus El Salvador, and supported by the observations of Douglas and Mohais (2009) that ground motion variability is higher in the Lesser Antilles than is captured by any single GMPE. Thus, for

the final selection, models were selected that both over and underpredict the observed ground motions in each of the tectonic regions. The GMPEs and their logic trees are shown in Table 9.

Notably, several recent GMPEs applicable to the tectonic region types in DOM21 have been developed since the CCARA project. During the first phase of the TREQ project, within which the DOM21 model was completed, these had not yet been implemented into the OpenQuake Engine and therefore could not be easily included in the GMC. However, these GMPEs are now available. Thus, we reviewed the GMPE selection and updated the subduction GMPEs for interplate and intraslab regions to include a newer model, Parker et al. (2020). In both cases, the oldest GMPE was replaced, both because they were outdated and because the GMPE of Parker et al. (2020) maintained the range and median intensity measure levels from the CCA GMC.

Table 9 Ground motion prediction equations (GMPE) and weights used in the DOM21 model.

Subduction Interface	**Weight**
AbrahamsonEtAl2015SInter	0.33
ZhaoEtAl2006SInter	0.33
ParkerEtAl2020SInter	0.34
Subduction IntraSlab	**Weight**
AbrahamsonEtAl2015SSlab	0.33
ParkerEtAl2020SSlab	0.33
Kanno2006Deep	0.34
Active Shallow Crust	**Weight**
AkkarEtAlRjb2014	0.33
CauzziEtAl2014	0.33
AbrahamsonEtAl2014	0.34

5 PSHA CALCULATION AND MAIN RESULTS

We use the OpenQuake Engine (Pagani et al., 2014) to calculate classical PSHA results covering the island of Hispaniola, and in more detail for some of the largest cities in the Dominican Republic. The results include:

- **Hazard curves**:
  - on rock ($v_{s,30}$ = 800 m/s) and for the soil conditions ($v_{s,30}$ computed from the topography using Allen and Wald (2007)
  - Intensity measure types (IMTs) for the peak ground acceleration (PGA) and the spectral acceleration (SA) with periods T=0.1, 0.2, 0.5, 1.0, and 2.0 seconds
  - mean, individual realizations (i.e., end branches of the logic tree), and the 16th and 84th quantiles
- **Hazard maps**:
  - mean PGA and SA with periods T=0.1, 0.2, 0.5, 1.0, and 2.0s on rock and for soil conditions
  - computed for probabilities of exceedance (POEs) of 2% and 10% in 50 years, equivalent to return periods of 2475 and 475 years, respectively
- **Uniform hazard spectra**:
  - mean values and the 16th and 84th quantiles
  - on rock and for soil conditions
  - computed for POEs of 2% and 10% in 50 years
- **Seismic hazard disaggregation**
  - for Santiago de los Caballeros and Santo Domingo
  - by (1) magnitude, distance, and GMPE epsilon and (2) latitude, longitude, and tectonic region type
  - on rock for 10% POE in 50 years

Here, we present a subset of these results, focusing especially on those that are of interest to the TREQ project.

5.1 Hazard curves, maps, and uniform hazard spectra

Figure 15, Figure 16, and Figure 17 show the hazard maps for PGA, SA(0.2s), and SA(1.0s), respectively, computed on rock for 10% and 2% POE in 50 years. In all cases, the hazard is highest near the fastest moving crustal faults: the Septentrionale fault in the north of the Dominican Republic, and the Enriquillo-Plantain Garden fault system that bisects the peninsula in the southwest of Haiti. Along these faults, PGA reaches 0.5 – 0.7g and 1.0 – 1.5g with 10% and 2% POE, respectively, in 50 years. Away from the major faults, the hazard is lower but persistent. PGA exceeds 0.2 and 0.4g for 10% and 2% POE, respectively, in 50 yrs across the majority of the island. The lowest hazard is in west-central Haiti. These patterns persist for SA(0.2s) and SA(1.0s). The highest intensity measure levels (IMLs) are computed for SA(0.2s), exceeding 3.0g along the faults with 2% POE in 50 years.

Figure 18 shows the hazard curves for four major cities in the Dominican Republic – Santo Domingo (the capital), Santiago de los Caballeros (herein also called "Santiago"), Bonoa, and Bani – and Port-au-

Prince, the capital of Haiti. This depiction shows how the relative hazard among the cities varies based on the considered probability of exceedance (i.e., the return period of the IMLs). The hazard curves are the means for six intensity measure types (IMTs) computed on reference rock. For all IMTs, the annual POEs for very low IMLs are comparable in all cities except Port-au-Prince, for which the POEs are slightly lower, which, notably, is close to where the hazard maps showed the highest hazard; on the other hand, for the two POEs indicated in the figures, the IMLs are *highest* here and in Santiago. This suggests a significant contribution by infrequent moderate to high magnitude earthquakes on the nearby crustal faults (described with the hazard maps) to the hazard computed for these POEs.

Figure 19 shows the uniform hazard spectra derived for each city and the indicated return periods in Figure 18, and Table 10 lists the values at each sampled point; these are complementary to Figure 18, and depict how the hazard levels at a site vary for buildings with different vibrational periods. In general, these are consistent with the hazard curves, and demonstrate that for all vibrational periods the expected shaking levels are highest in Santiago and Port-au-Prince.

Table 10. Mean intensity measure levels (g) computed on reference rock for PGA and five spectral periods for 10% and 2% POE in 50 years.

City	PGA (g) 10%/2%	SA(0.1) (g) 10%/2%	SA(0.2) (g) 10%/2%	SA(0.5) (g) 10%/2%	SA(1.0) (g) 10%/2%	SA(2.0) (g) 10%/2%
Santiago de los Caballeros (DR)	0.51/0.99	1.11/2.21	1.10/2.19	0.61/1.26	0.33/0.70	0.16/0.35
Port-au-Prince (HA)	0.54/1.20	1.19/2.81	1.12/2.55	0.57/1.32	0.29/0.68	0.14/0.33
Santo Domingo (DR)	0.26/0.53	0.63/1.25	0.58/1.13	0.30/0.60	0.16/0.31	0.08/0.15
Bonao (DR)	0.29/0.55	0.68/1.32	0.62/1.20	0.34/0.66	0.18/0.37	0.09/0.158
Bani (DR)	0.32/0.62	0.77/1.55	0.69/1.35	0.33/0.66	0.17/0.33	0.08/0.16

The results displayed so far have depicted mean hazards, i.e., a single weighted-average result of the full seismic source and ground motion model logic trees. However, it is also instructive to review the full range of values permitted by the input models. Figure 20 shows the PGA hazard curves on rock for each logic tree end branch (i.e., a "realization") for the city of Santiago (70.6931°W, 19.4792°N), as well as the mean PGA computed from the weighted average of each realization. The figure reveals that the PGA with a 10% POE in 50 years span >0.2g around the mean value of 0.5g, and ~0.4g for 2% POE in 50 years around the mean value of 0.99g. Additionally, the distribution of hazard values at 2% POE in 50 years is bimodal, indicating that one epistemic uncertainty, most likely the weighting schematic used to construct the distributed seismicity sources, is having a significant impact on the hazard.

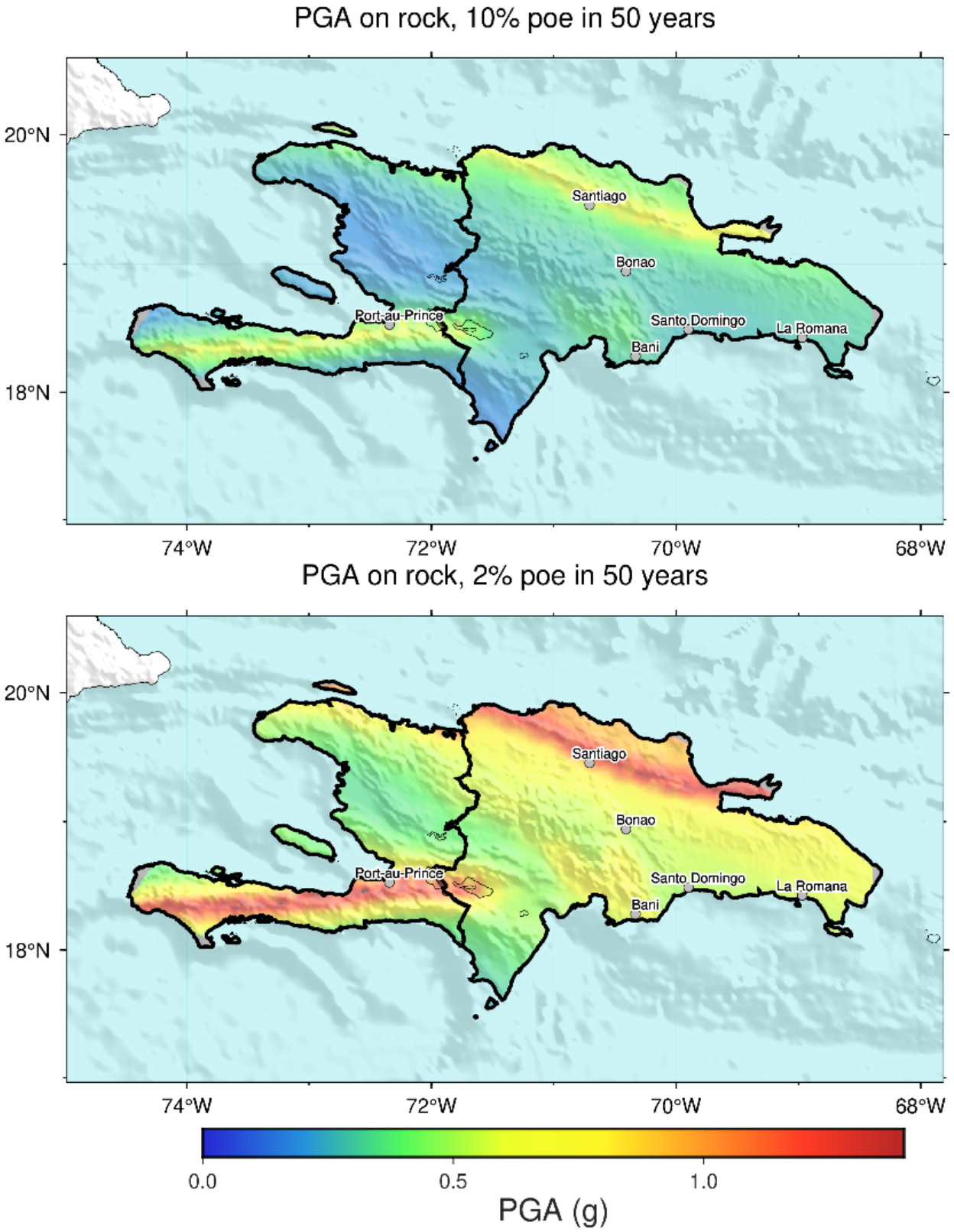

Figure 15 Seismic hazard map of mean peak ground acceleration (PGA) computed for (top) 10% probability of exceedance and (bottom) 2% probability of exceedance in 50 years.

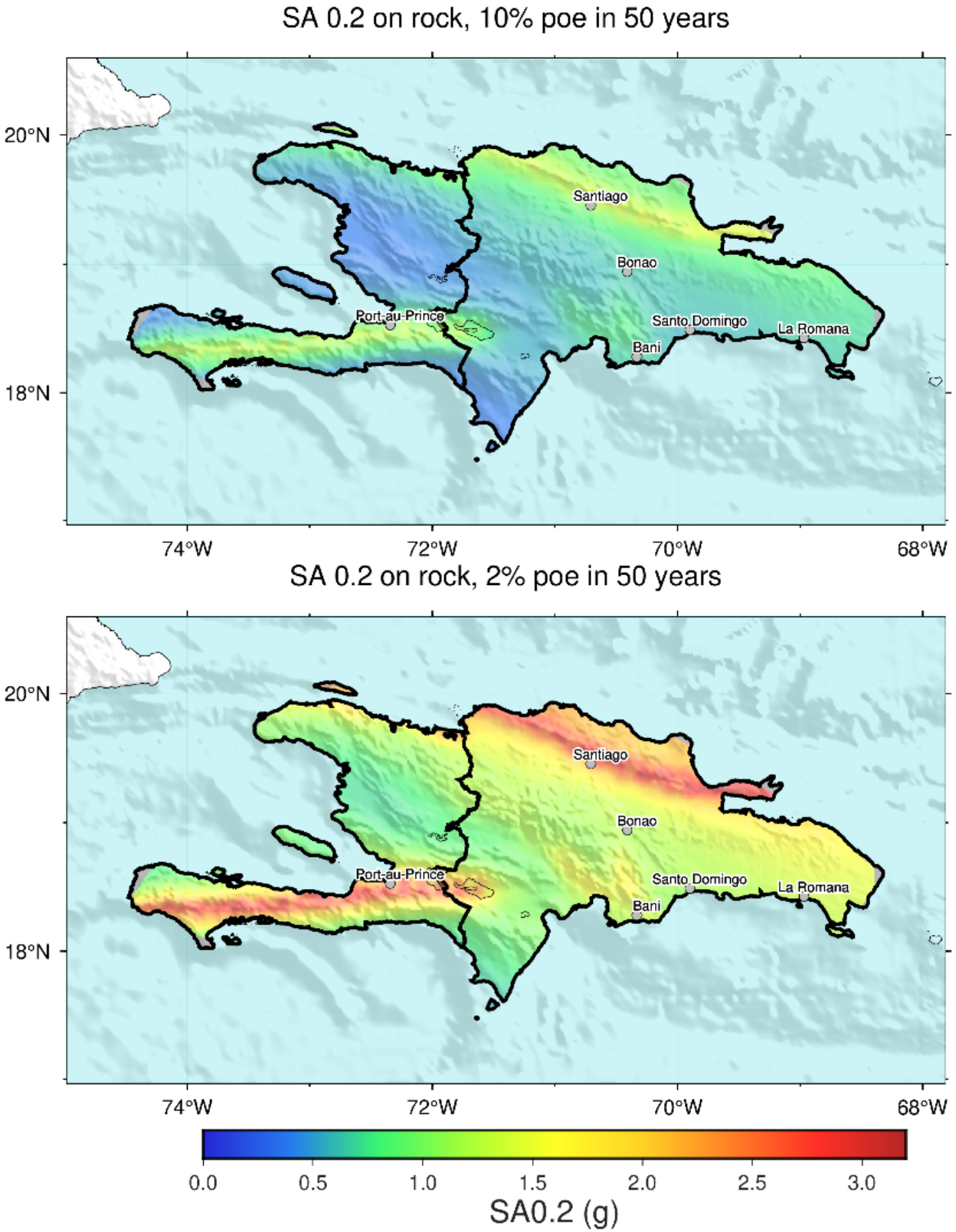

Figure 16. Seismic hazard map of spectral acceleration (SA) with period T=0.2s computed for (top) 10% probability of exceedance and (bottom) 2% probability of exceedance in 50 years.

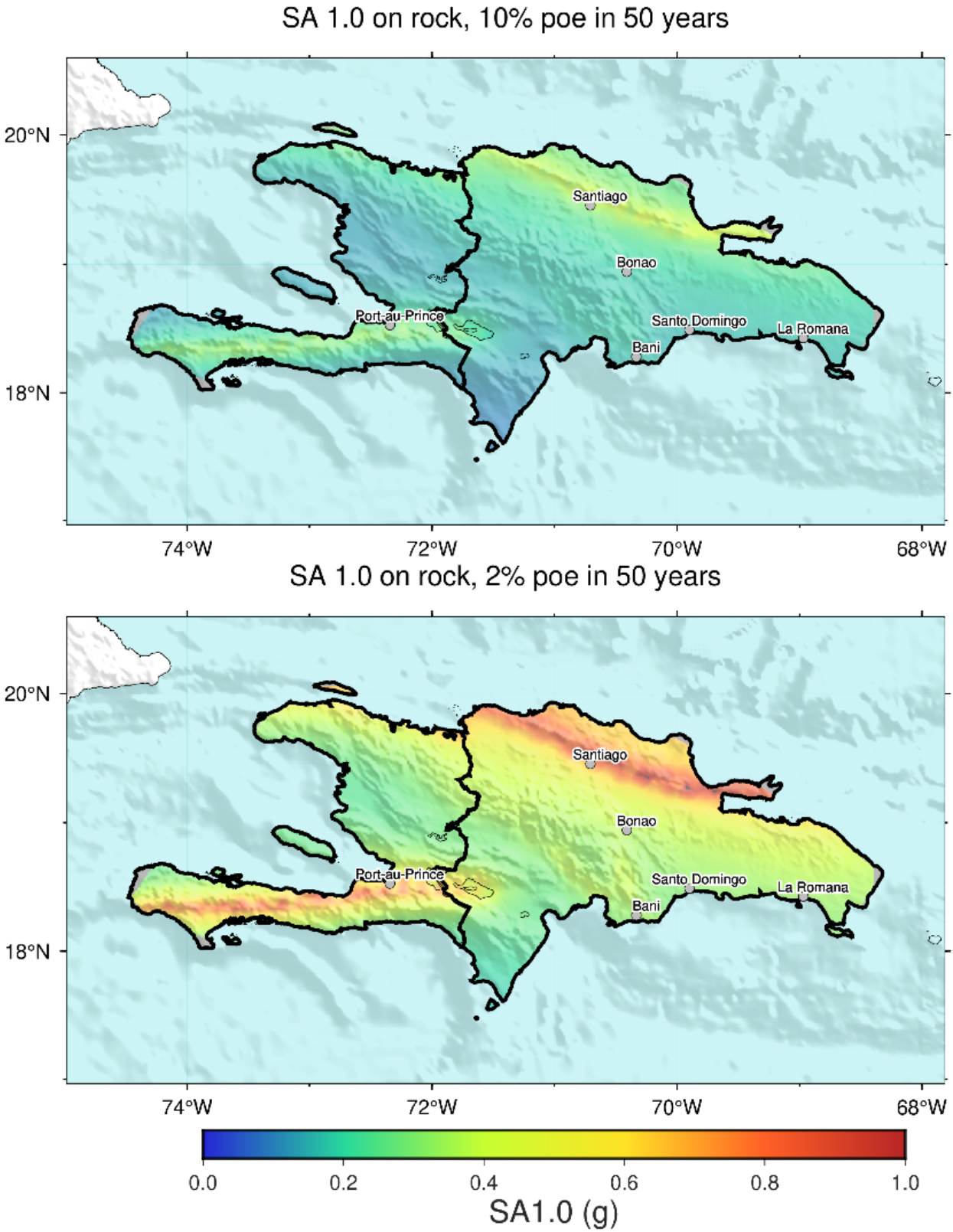

Figure 17 Seismic hazard map of spectral acceleration (SA) with period T= 1.0s computed for (top) 10% probability of exceedance and (bottom) 2% probability of exceedance in 50 years.

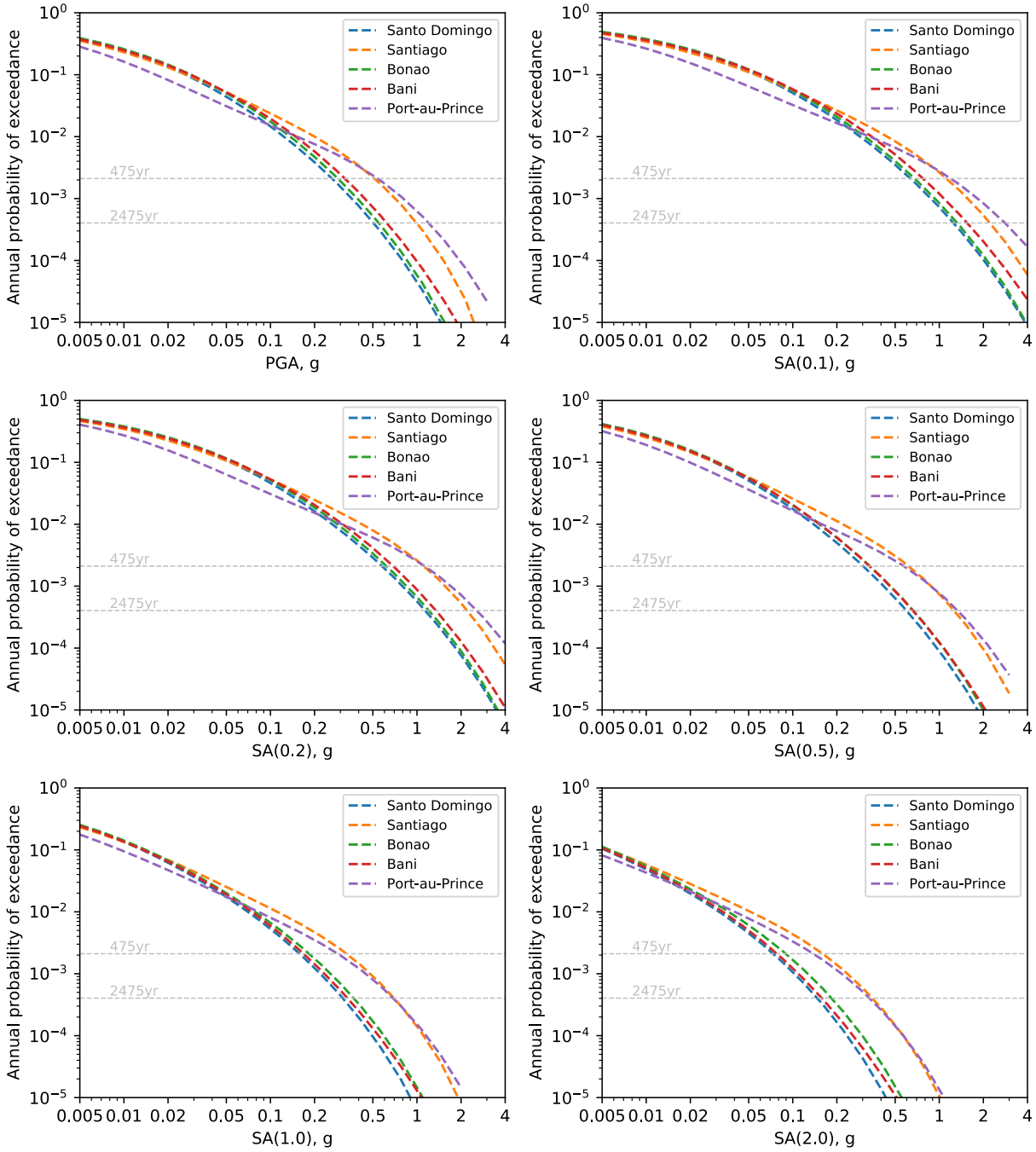

Figure 18 Seismic hazard curves for major cities in the Dominican Republic and Port-au-Prince, Haiti. Intensity measure types are indicated on the x-axis and include PGA and spectral accelerations with the specified period. All plots show mean hazard computed for reference rock conditions. Dashed grey lines show the 475 and 2475 year return periods, corresponding to 10% and 2% POE in 50 years, respectively. Note: in most cases the Santo Domingo and Banao hazard curves are very similar, and one is occluded from view by the other.

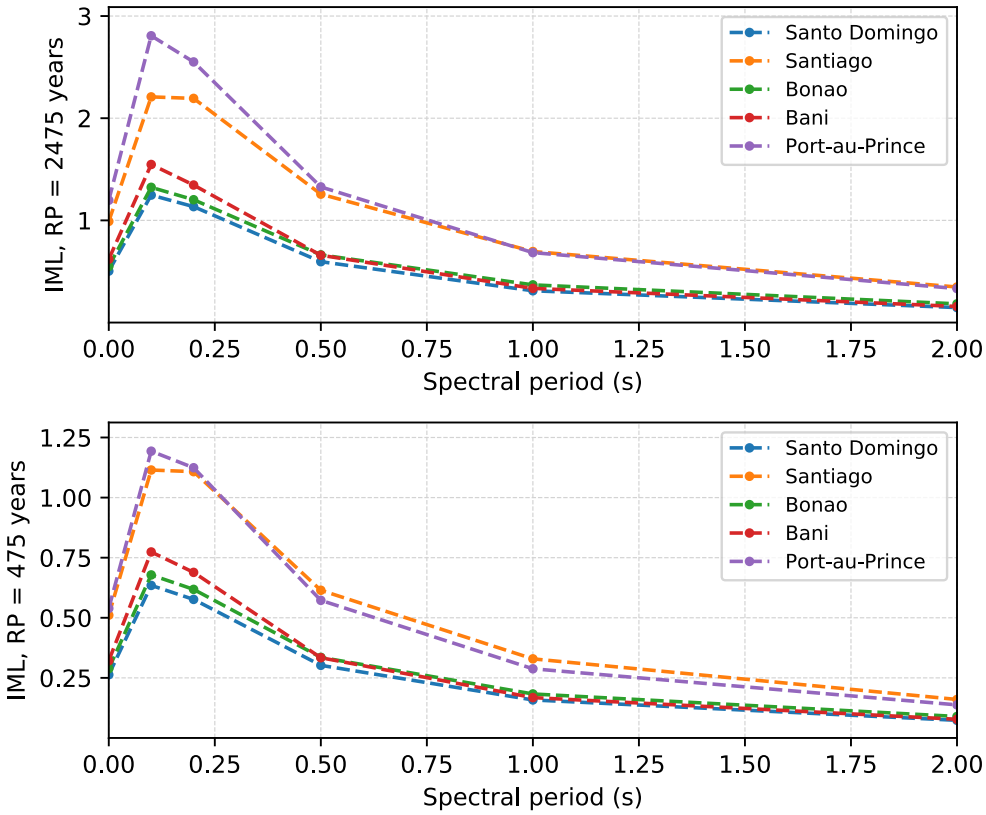

Figure 19 Uniform hazard spectra (UHS) (mean on rock) for major cities at (top) 2475 years, and (bottom) 475 years. Note: in most cases the Santo Domingo and Banao hazard curves are very similar, and one is occluded from view by the other.

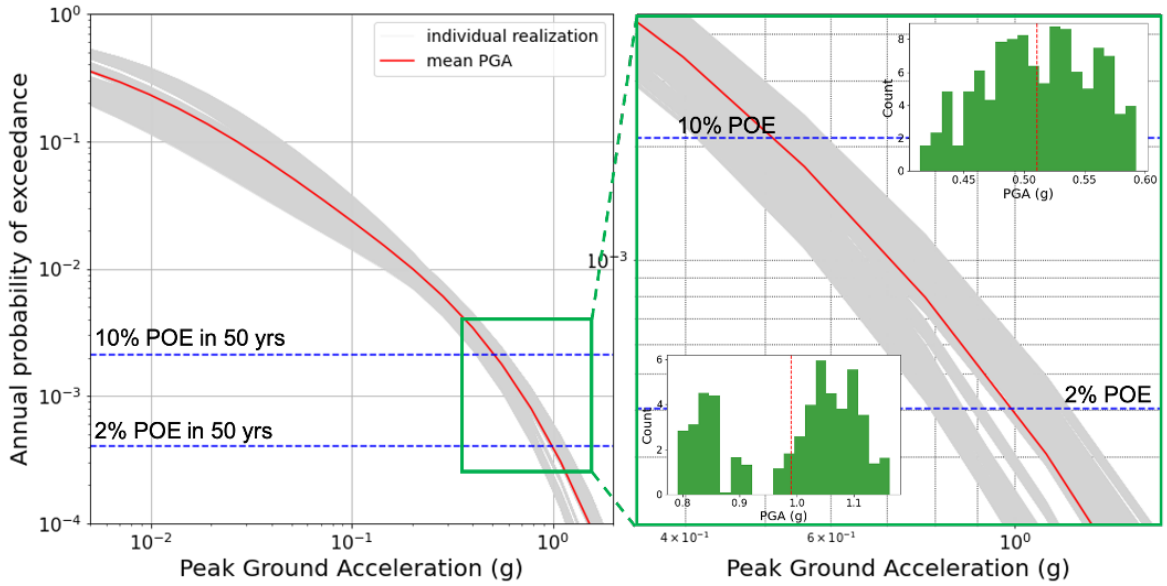

Figure 20 Range of PGA values computed on rock for Santiago de los Caballeros. Left: PGA hazard curves for the individual realizations (gray) compared to the mean (red). Blue dashed lines indicate the 10% and 2% POE in 50 years. Right: As shown in left, but zoomed in to the plot area covered by the green box to better show the range of hazard curves permissible by the model. Histograms show the normalized count of hazard values for 20 bins spanning the total PGA distribution of each POE (green), not accounting for the weight of each realization, and the mean PGA (red).

5.2 Disaggregation

Seismic hazard disaggregation reveals which combinations of explanatory variables (e.g., magnitude and distance) are contributing most to the ground motion parameter level at a site for a specific IMT and POE. In other words, disaggregation indicates which sources, grouped by their controlling parameters, are controlling the hazard for a given return period. Here, we disaggregated hazard following Pagani and Marcellini (2007) in terms of PGA for both 10% and 2% POE in 50 years for the cities of Santiago and Santo Domingo in terms of: (1) position (latitude and longitude bins) and tectonic region type; and (2) magnitude, distance, and GMPE epsilon.

Figure 21 shows the disaggregation results for Santiago, revealing that the hazard for PGA at both return periods (10% and 2% in 50 years corresponding to 475 and 2475 years) is dominated by nearby active shallow crustal (ASC) sources with small contributions from the Subduction Interface. In particular, ASC sources <25 km from Santiago and with M_W ~ 6.5-8.0 dominate the hazard, while those just as close with M_W ~ 6.0-6.5 or more distant (but still within 50 km) M_W > 8.0 events also contribute. At 2% in 50 years, the impact of the GMPE aleatory variable is clear, since all contributions have large (relative to the range) positive values of epsilon. From the results, we infer that the Septentrionale fault and its associated off-fault controls the ground shaking hazard in Santiago for the return periods of interest. The Subduction Interface contributions are from the North Hispaniola Trench, and may have a greater impact when disaggregating for other intensity measure types (i.e., longer periods).

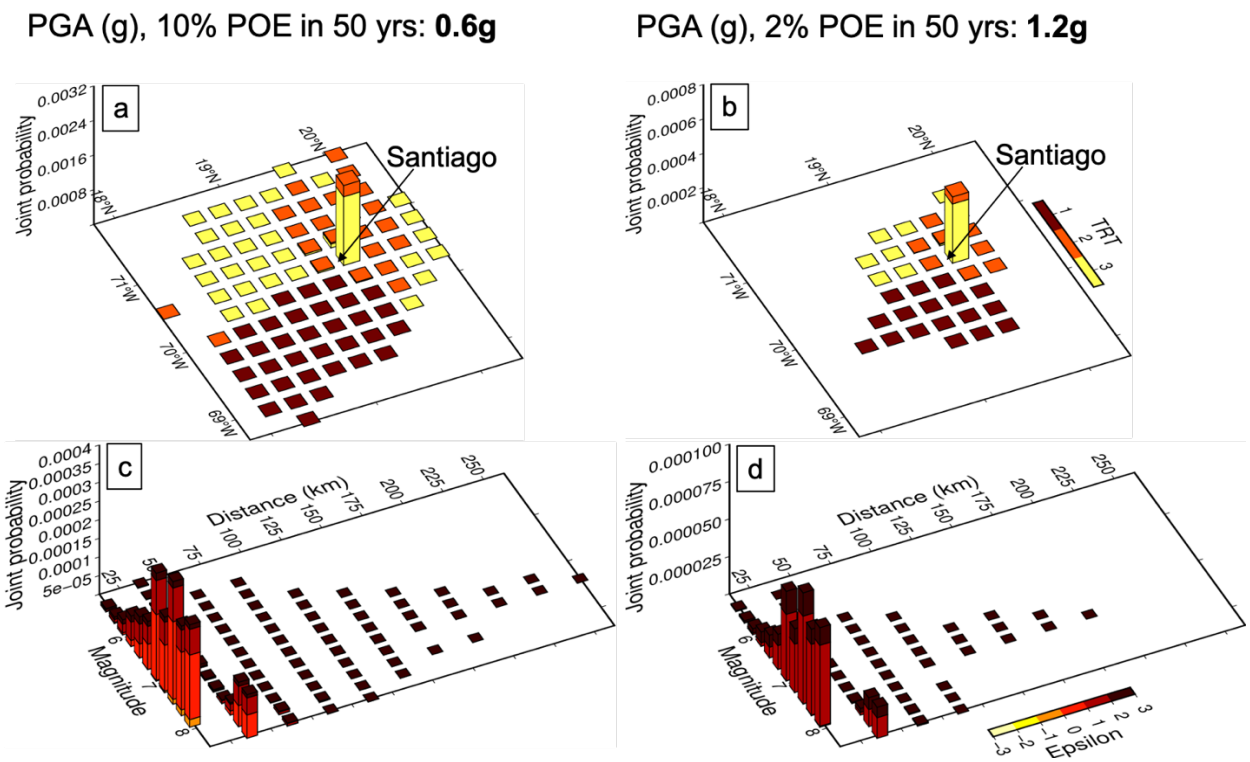

Figure 21 Disaggregation of mean PGA on rock for Santiago, 10% and 2% POE in 50 years (a,c and b,d, respectively). (a) and (b) are disaggregated by latitude, longitude, and tectonic region type (TRT). Only binned contributions with joint probabilities > 1E-16 are plotted. TRTs: 1 (brown) = Subduction Intraslab, 2 (red) = Subduction Interface, and 3 (yellow) = Active Shallow Crust. (c) and (d) are disaggregated by magnitude, distance, and epsilon (the GMPE inter-event term).

Figure 22 and Figure 23 shows the disaggregation results for Santo Domingo. Santo Domingo is uniquely positioned in close proximity to several structures in the ASC as well as two of the three subduction zones included in the present model: the Los Muertos Trench in the south and the North Hispaniola Trench to the north, the latter of which includes both interface and intraslab sources. Some spatial bins include all three TRTs, and indeed all three TRTs contribute to the ground shaking hazard observed in Santo Domingo at both 10% and 2% POE in 50 years, with the ASC contributing the most. However, as in Santiago, the relative contributions of the three TRTs is likely to change for other intensity measure types. The disaggregation by magnitude, distance, and GMPE epsilon also shows contributions from wide parameter ranges. Sources with magnitudes M_W 5.0-6.0 within 50 km contribute most to the hazard, and are seconded by larger ruptures (M_W > 8.0; subduction interface sources) between 50 and 100 km from Santo Domingo. M_W ~ 6.5–7.5 earthquakes coming from both types of subduction sources continue to have notable contributions beyond 100 km. The main patterns persist for both 10% and 2% in 50 years, but – like for Santiago – more contribution is coming from the highest values of epsilon for 2% in 50 years.

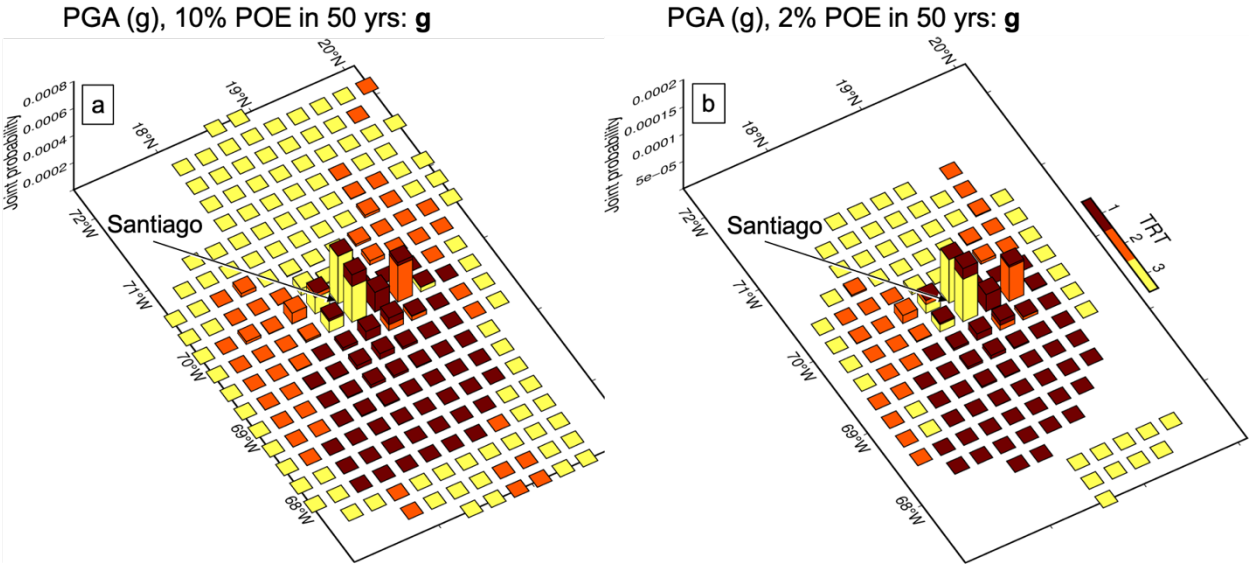

Figure 22 Disaggregation of mean PGA on rock for Santo Domingo, (a) 10% and (b) 2% POE in 50 years. Disaggregation is by latitude, longitude, and tectonic region type (TRT). Only binned contributions with joint probabilities > 1E-16 are plotted. TRTs: 1 (brown) = Subduction Intraslab, 2 (red) = Subduction Interface, and 3 (yellow) = Active Shallow Crust.

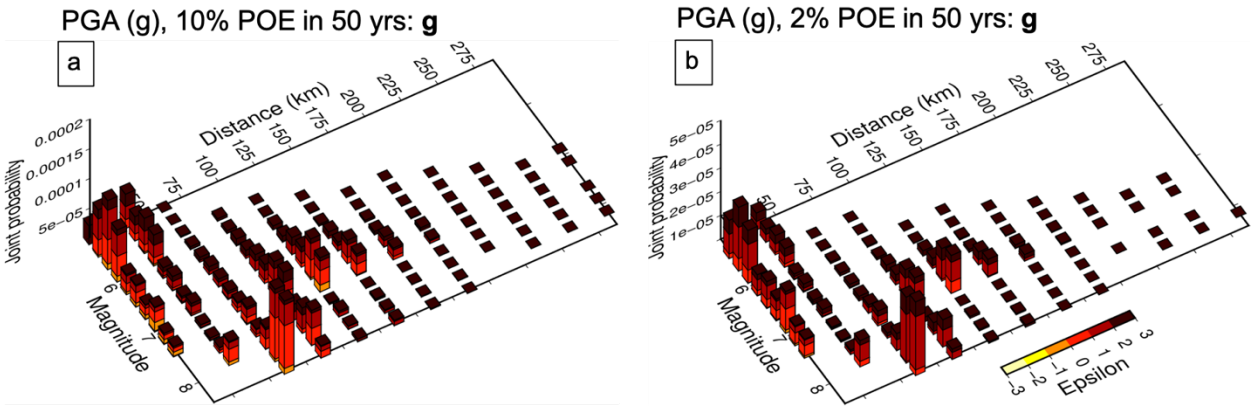

Figure 23 Disaggregation of mean PGA on rock for Santo Domingo, (a) 10% and (b) 2% POE in 50 years. Disaggregation is by magnitude, distance, and epsilon (the GMPE inter-event term). Only binned contributions with joint probabilities > 1E-16 are plotted.

6 Discussion and Conclusions

6.1 Comparison to former models

In the introduction, we described several former works that have studied the seismic hazard in Hispaniola. In this section, we compare the results from the present model to the hazard computed from the overlapping coverage of four past studies: GEM's updated CCARA model covering the Caribbean and Central America, the model by Frankel et al., (2011) covering Haiti and parts of the Dominican Republic, and microzonations covering Santiago (Bertil et al., 2010) and Santo Domingo (Bertil et al., 2015).

6.1.1 CCARA

An updated version of the PSHA model resulting from the Caribbean and Central America Risk (CCARA) Project covers Hispaniola in GEM's Global Hazard Mosaic (Pagani et al., 2020b); herein, this updated version is called CCA. This model provides complete geographic coverage of Hispaniola, but does not include epistemic uncertainties in the source model. Because GEM led the development of the CCA model, it can be most easily compared to the present model (herein called DOM21) for Hispaniola.

We perform broad comparisons on the observed differences in spatial patterns between CCA and DOM21, focusing on mean PGA on rock with a 10% POE in 50 years (here termed "hazard"). The hazard is overall higher for CCA; for example, at the easternmost of Hispaniola, and in general along the southern coast of the Dominican Republic, CCA hazard exceeds DOM21 hazard by ~0.2g (e.g., 0.2-0.4g for DOM21 vs 0.35-0.55g for CCA), increasing to a discrepancy almost 0.3g in west-central Haiti. On the other hand, the hazard close to some faults is higher in the DOM21 model. Along the Septentrionale fault, the CCA model shows comparable peak values to those of DOM21, but for DOM21 the values ranging ~0.5-0.7 cover a larger swath – points where CCA computes values as low as ~0.45g. The discrepancy along the Enriquillo-Plantain Garden fault system is similar. The same spatial patterns persist for mean PGA on rock with 2% POE in 50 years, with differences between DOM21 and CCA increasing to ~0.4 g.

We zoom in to Santiago and Santo Domingo to look more closely at other hazard metrics. Figure 24 shows the UHS for Santiago and Santo Domingo, comparing the DOM21 mean PGA and the 84th and 16th quantiles for 10% and 2% POE to that from CCA. Recall from the disaggregation results that Santiago is located close to the Septentrionale fault, and that this fault as well as associated crustal seismicity control the hazard; however, Santiago is far enough from the fault itself to approach the geographic region where CCA shows higher hazard than DOM21. Thus, the mean intensity measure levels from the two models are close (mostly within ~10%) for the 10% POE in 50 years results, and diverge by only slightly more for 2% POE in 50 years. The CCA results are within the 84th and 16th quantiles of DOM21 except for period T=2.0s. CCA shows higher mean values for the shorter periods (T<0.5s), while DOM21 shows higher values at longer periods. On the other hand, Santo Domingo is on the southern coast of the Dominican Republic, where the PGA spatial patterns show that hazard in DOM21 is much lower than in CCA. This is consistent across all spectral periods and both return periods, and in all cases the CCA values are outside of the 84th quantile for DOM21. Often, CCA values for 10% POE in 50 years are closer to the DOM21 values for 2% POE in 50 years.

The reasons for the discrepancies between the two models result from the seismic source characterization (SSC), since the ground motion characterization used for both models is the same. Some aspects of the SSC in CCA are similar to the source modelling approach used in DOM21. For example, some of the subduction zones in both PSHA input models use the catalogue classification and subduction source modelling approach by Pagani et al., (2020a), and the active shallow crustal seismicity is modelled by a combination of distributed seismicity (point sources with smoothed rates) and faults. However, the DOM21 model was able to incorporate more recent and complete earthquake catalogues and active faults data than CCA; used the SHERIFS approach – a more advanced approach to modelling faults; and accounted for some of the epistemic uncertainties in seismicity sources, rates, and distribution. Additionally, the DOM21 model smoothed the intraslab seismicity rates based on past occurrences, while the CCA model used uniform rates across the slab volume. Recall from the seismic disaggregation that all tectonic region types contributed to the hazard in Santo Domingo. Uniform seismicity rates would have modelled more intraslab seismicity in the spatial bins underlying Santo Domingo, increasing the computed hazard.

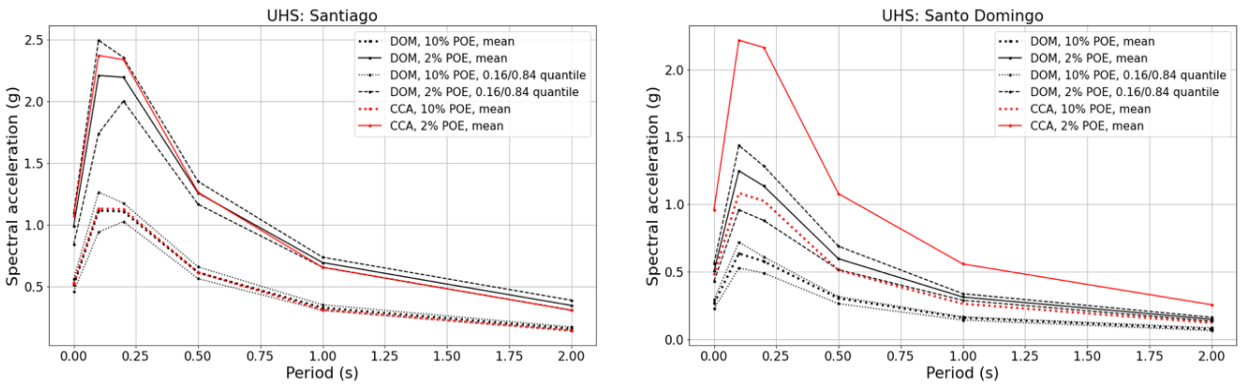

Figure 24 Uniform hazard spectrum on rock comparing the mean, 84th, and 16th quantiles computed from the DOM model to the mean computed using CCA for (left) Santiago and (right) Santo Domingo.

6.1.2 PSHA for Haiti (Frankel et al., 2011)

The hazard model produced by Frankel et al. (2011) was developed by the USGS as part of the response to the M_W 7.0 earthquake that devastated Haiti in 2010. The model in general uses a similar approach to the one used for DOM21, using seismicity and active faults data to develop seismic source models that represent the crustal faults, subduction zones, and active shallow crustal earthquakes.

We compare the mean PGA on rock computed from DOM21 to the maps in Figures 3 and 4 in Frankel et al. (2011). For both 10% and 2% POE in 50 years, the hazard patterns between the two maps are similar. Despite using different ground motion model logic trees, in particular for the active shallow crustal sources, PGA values computed from DOM21 near the Enriquillo-Garden Plantain fault and the Septentrionale fault are close to those from the Frankel et al. (2011) model, however, they cannot be precisely evaluated since the Frankel et al. (2011) maps use a color scale that spans 0.1 – 0.8g in the areas of interest. On a finer scale, the patterns differ slightly, for example near Bani where the DOM21 hazard is higher. Here, and throughout much of the interior of Hispaniola, the DOM21 model includes crustal faults for which data was not available to Frankel et al. (2011); accordingly, the authors note that the understanding of hazard will change as more fault data becomes available, as it has for the preparation of the DOM21 model. Similarly, Frankel et al. (2011) indicate that their information was less complete for the Dominican Republic than for Haiti.

6.1.3 Microzonation of Santiago de los Caballeros (Bertil et al., 2010)

The microzonation of Santiago, developed by Bertil et al. (2010), covers the city of Santiago. Like the model of Frankel et al. (2011), the seismic source characterization used for the microzonation includes the Septentrionale fault, the Enriquillo-Plantain Garden fault, and the subduction zones to the north and south of the island, but at the time of development did not have as much information about other faults as were available from the SGN fault database for developing the DOM21 model. Overall, the approach used to produce the two models is similar. The microzonation uses faults and background seismicity, and considers a range of values for some source parameters in the logic tree.

Here, we compare the range of values computed for Santiago by Bertil et al. (2010) to those computed by the DOM21 model. The two studies have the same spatial pattern: hazard decreases along contours that parallel the Septentrionale fault as the distance from the fault increases. The mean PGA on rock computed from Bertil et al. (2010) is lower than that of DOM21. At 10% POE in 50 years, the microzonation model ranges from ~0.33 – 0.44 g across the city, while DOM21 ranges from ~0.45 – 0.61. The discrepancy is larger for 2% POE in 50 years, where the microzonation shows PGA ~0.55 – 0.72g, while the DOM21 model ranges ~0.88 – 1.20g.

We additionally compare the UHS for 10% POE in 50 years at site N.27 (70.6563 W, 19.4725 N) in Bertil et al. (2010); seeFigure 25. Like PGA, all spectral periods in the DOM21 model are close to 50% larger than the microzonation. This trend persists for the mean as well as the 85th and 15th quantiles, without any overlap between the given ranges.

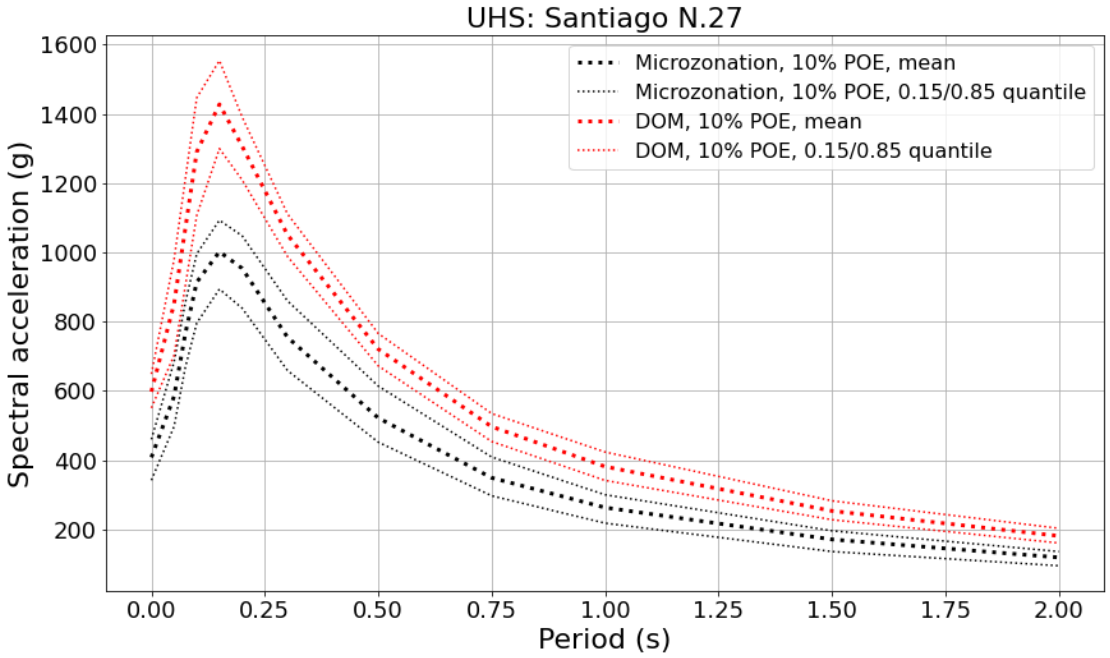

Figure 25 UHS for 10% POE in 50 years at Site N.27 from the Bertil et al. (2010) microzonation and the DOM21 model. The microzonation values are taken from Table 9 of Bertil et al. (2010).

To understand one possible reason why the hazard is higher from the DOM21 model, we compare the MFDs of the Septentrionale fault, the structure controlling hazard in Santiago. The MFD occurrence rates are lower in the DOM21 version than in the microzonation study, however, the spatial distribution of the sources varies. The microzonation concentrates the majority of the seismicity on the fault itself, only permitting occurrences up to M_W 5.5 in the zone of background seismicity surrounding the fault. On the contrary, the DOM21 model allows earthquakes up to M_W 7.0 – and in some branches up to M_W 7.5 in the smoothed seismicity. Thus, large earthquakes in DOM21 occur closer to Santiago.

6.1.4 **Microzonation of Santo Domingo (Bertil et al., 2015)**

The microzonation study of Bertil et al. (2015) covers the city of Santo Domingo. The source model was developed using an improved methodology compared to the Santiago microzonation (Bertil et al., 2011) that was made possible by more available fault data, as well as more seismicity and geophysical data. In particular, the study was able to incorporate some faults in the active shallow crust that are close to Santo Domingo, and used two source model logic tree branches: one of which uses faults and background seismicity, while the other uses area source zones. The source models incorporate uncertainties for some parameters in the logic tree.

We compare the spatial distribution of mean PGA computed from the microzonation to the DOM21 model. The DOM21 model shows slightly higher hazard at both return periods. The DOM21 model shows PGA with 10% POE in 50 years is ~constant at 0.26g across the city, while the microzonation shows ~0.19 – 2.3g, increasing from southwest to northeast. For 2% POE in 50 years, DOM21 shows ~0.48 – 0.52g across the city, while in the microzonation, the hazard increases from ~0.35 – 0.42g from southwest to northeast.

We also compare the UHS for one point within the city: site MOPC, which is approximately central to the study area of Bertil et al. (2015); see Figure 26. Like PGA, the mean values for all spectral periods in the DOM21 model are larger than those from the microzonation. This trend persists for the mean as well as the 85th and 15th quantiles. Contrary to what is observed for Santiago, the ranges from the two models do overlap. The range of PGA values computed from the microzonation is much larger than that computed from DOM21, and in some cases (i.e., the periods longer than 0.2s) the microzonation values at the 85th quantile exceed the mean or even 85th quantile from DOM21.

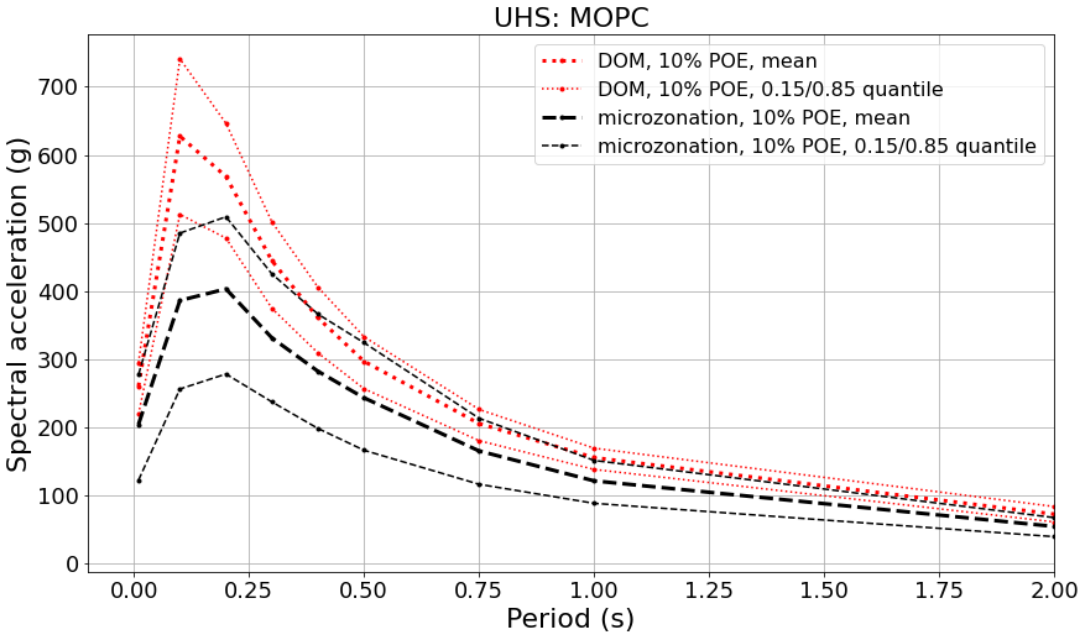

Figure 26. UHS for 10% POE in 50 years at the MOPC site from the Bertil et al. (2015) microzonation and the DOM21 model. The microzonation values are taken from Table 14 of Bertil et al. (2015).

We consider some explanations for the discrepancies in the results from the two models. The parameters for which epistemic uncertainties are considered in the microzonation source model are more straightforward (e.g., MFD a- and b-values and M_{max} of the sources) than those of the DOM21 model (e.g., the same uncertainties but incorporated via the SHERIFS algorithm and the smoothing approach). Additionally, while the microzonation for Santo Domingo (Bertil et al., 2015) includes more faults than for Santiago (Bertil et al., 2011), the DOM21 model still includes a few more, some of which are just west of Santo Domingo and may be the reason that a gradient in hazard is not observed as strongly across the city. Like for Santiago, the M_{max} of earthquakes in the background is M_W = 5.5 for the microzonation source model that uses both faults and distributed seismicity, while higher values are allowed in DOM21. Finally, the GMC used for the microzonation is different from the one used by DOM21.

6.1.5 Comparison to other models: summary

Among all the models described above, with the exception of the CCA model, the major characteristics of the spatial patterns of hazard are comparable, despite the models being developed by different authors, using datasets with different levels of completeness, and with different applications or study

regions in mind. In general, we consider this to support the results of the DOM21 model, despite the differences in absolute hazard value.

6.2 Initial applications of DOM21 model

The DOM21 PSHA model covering the island of Hispaniola was prepared as part of the TREQ Project. The first application of the model is an urban hazard assessment for Santiago de los Caballeros, which is covered by TREQ deliverable *"D2.2.4. Seismic hazard analysis at the urban scale".*

7 REFERENCES

Abrahamson, N. A., Gregor, N., and Addo, K. (2016). BC Hydro Ground Motion Prediction Equations for Subduction Earthquakes. Earthquake Spectra, 32(1), 23-44. doi:10.1193/051712eqs188mr

Abrahamson, N. A., W. J. Silva, and R. Kamai (2014). Summary of the ASK14 ground motion relation for active crustal regions, Earthq. Spectra 30, 1025–1055.

Akkar S., M. A. Sandikkaya, and J. J. Bommer (2014). Empirical Ground-Motion Models for Point- and Extended- Source Crustal Earthquake Scenarios in Europe and the Middle East, Bulletin of Earthquake Engineering (2014), 12(1): 359 - 387

Atkinson Gail M. and David M. Boore (2006). Earthquake Ground-Motion Prediction Equations for Eastern North America; Bulletin of the Seismological Society of America, Volume 96, No. 6, pages 2181-2205

Atkinson G. M. and D. M. Boore (2003). Empirical ground-motion relations for subduction zone earthquakes and their application to Cascadia and other regions. Bulletin of the Seismological Society of America, 93(4):1703-1729, 2003.

Benford, B., DeMets, C., Calais, E. (2012). GPS estimates of microplate motions, northern Caribbean: evidence for a Hispaniola microplate and implications for earthquake hazard. Geophys. J. Int. 191 (2), 481–490.

Bertil D., Terrier M., Belvaux M. (2015) – Análisis de las fuentes sísmicas y evaluación de la amenaza sísmica regional del gran Santo Domingo. "Estudio de la amenaza sísmica y vulnerabilidad física del Gran Santo Domingo" - Actividad 1.1. BRGM/RP-65305-FR, 149 p., 85 fig., 26 tablas.

Bertil D., Lemoine A., Winter T., Belvaux M. (2010) – Microzonificación sísmica de Santiago – Republica Dominicana. Amenaza regional. Informe final. BRGM/RC-59107-FR, 100 p., 36 fig., 12 tablas, 2 anexos.

Bommer JJ, Douglas J, Scherbaum F, Cotton F, Bungum H, Fäh D (2010). On the selection of ground-motion prediction equations for seismic hazard analysis. Seismol Res Lett 81:783–793

Boore David M., Jonathan P. Stewart, Emel Seyhan and Gail Atkinson (2014). NGA-West2 Equations for Predicting PGA, PGV, nd 5 % Damped PGA for Shallow Crustal Earthquakes; Earthquake Spectra, Volume 30, No. 3, pages 1057 - 1085.

Castro, R. R., Fabriol, H., Bour, M., & Le Brun, B. (2003). Attenuation and site effects in the region of Guadeloupe, Lesser Antilles. Bulletin of the Seismological Society of America, 93(2), 612-626.

Calais, E., Symithe, S., de Lépinay, B., Prépetit, C. (2016). Plate boundary segmentation in the northeastern Caribbean from geodetic measurements and Neogene geological observations. Comptes Rendus Geoscience. 348. 10.1016/j.crte.2015.10.007.

Calais, E., A. Freed, G. Mattioli, F. Amelung, S. Jónsson, P. Jansma, S.-H. Hong, T. Dixon, C. Prépetit, and R. Momplaisir (2010), Transpressional rupture of an unmapped fault during the 2010 Haiti earthquake, Nature Geoscience, 3(11), 794-799.

Cauzzi C., E. Faccioli, M. Vanini, and A. Bianchini (2015). Updated predictive equations for broadband (0.01-10s) horizontal response spectra and peak ground motions, based on a global dataset of digital acceleration records. Bulletin of Earthquake Engineering, 13(6):1587-1612. doi: 10.1007/s10518-014-9685-y.

Chartier, T., Scotti, O., & Lyon-Caen, H. (2019). SHERIFS: Open-Source Code for Computing Earthquake Rates in Fault Systems and Constructing Hazard Models. Seismological Research Letters.

Cotton, F., Scherbaum, F., Bommer, J. J. and Bungum, H. (2006). Criteria for selecting and adjusting ground-motion models for specific target regions: Application to central Europe and rock sites, J. Seism., 10:2, 137-156.

DeMets, C., Gordon, R.G., Argus, D.F. (2010). Geologically current plate motions. Geophys. J. Int. 181, 1–80. http://dx.doi.org/10.1111/j.1365-246X.2009.04491.x.

DeMets, C., Jansma, P.E., Mattioli, G.S., Dixon, T.H., Farina, F., Bilham, R., Calais, E. & Mann, P. (2000). GPS geodetic constraints on Caribbean-North America plate motion, Geophys. Res. Lett., 27, 437–440, doi:10.1029/1999GL005436.

Douglas, J., & Mohais, R. (2009). Comparing predicted and observed ground motions from subduction earthquakes in the Lesser Antilles. Journal of Seismology, 13(4), 577-587.

Draper, G. (2008). Some speculations on the Paleogene and Neogene tectonics of Jamaica. Geological Journal, 43(5), 563-572.

Ekström, G., M. Nettles, and A. M. Dziewonski (2012). The global CMT project 2004-2010. Centroid-moment tensors for 13, 017 earthquakes, Phys. Earth Planet. Inter., 200-201, 1-9, 2012. doi:10.1016/j.pepi.2012.04.002

Frankel, A. (1995). Mapping seismic hazard in the central and eastern United States. Seismological Research Letters, 66(4), 8-21.

Frankel, A., Harmsen, S., Mueller, C., Calais, E., & Haase, J. (2011). Seismic hazard maps for Haiti. Earthquake Spectra, 27(1_suppl1), 23-41.

Garcia, J. and V. Poggi (2017a). A harmonized Earthquake Catalogue for Central America and the Caribbean region. CCARA Project. GEM Technical Report, Pavia, July 2017,

Garcia, J. and V. Poggi (2017b). A database of focal mechanisms for Central America and the Caribbean region. CCARA Project. GEM Technical Report, Pavia, July 2017,

Gardner, J. K., and L. Knopoff (1974). Is the sequence of earthquakes in southern California, with aftershocks removed, Poissonian? Bull. Seismol. Soc. Am. 64: 1363–1367.

Hayes, G. P., Moore, G. L., Portner, D. E., Hearne, M., Flamme, H., Furtney, M., & Smoczyk, G. M. (2018). Slab2, a comprehensive subduction zone geometry model. Science, 362(6410), 58-61.

Hippolyte, J.-C., Mann, P., and Grindlay, N. R. (2005). Geologic evidence for the prolongation of active normal faults of the Mona rift into northwestern Puerto Rico, in: Special Paper 385: Active Tectonics and Seismic Hazards of Puerto Rico, the Virgin Islands, and Offshore Areas, vol. 385, Geological Society of America, Boulder, Colorado, USA, 161–171, https://doi.org/10.1130/0-8137-2385-X.161.

Jansma, P.E., and Mattioli, G.S. (2005). GPS results from Puerto Rico and the Virgin Islands: Constraints on tectonic setting and rates of active faulting, in Mann, P., ed., Active Tectonics and Seismic Hazards of Puerto Rico, the Virgin Islands, and Offshore Areas: Geological Society of America Special Paper 385, p. 13–30.

Johnson, K. L., Pagani, M., & Styron, R. H. (2021). PSHA of the southern Pacific Islands. Geophysical Journal International, 224(3), 2149-2172.

Kanno T., A. Narita, N. Morikawa, H. Fujiwara, and Y. Fukushima (2006). A new attenuation relation for strong ground motion in Japan based on recorded data. Bulletin of the Seismological Society of America, 96(3): 879-897. doi: 10.1785/0120050138.

Leonard, M. (2010). Earthquake fault scaling: Relating rupture length, width, average displacement, and moment release, Bull. Seismol. Soc. Am. 100, no. 5A, 1971–1988.

Leroy, S., Ellouz-Zimmermann, N., Corbeau, J., Rolandone, F., de Lépinay, B. M., Meyer, … Muñoz, S. (2015). Segmentation and kinematics of the North America-Caribbean plate boundary offshore Hispaniola, Terra Nova, 27, 467–478, https://doi.org/10.1111/ter.12181.

Manaker, D. M., E. Calais, A. M. Freed, S. T. Ali, P. Przybylski, G. S. Mattioli, P. Jansma, C. Prépetit, and J. B. De Chabalier (2008). Interseismic plate coupling and strain partitioning in the northeastern Caribbean, Geophys. J. Int., 174(3), 889–903.

Mann, P., Burke, K., and Matumoto, T. (1984). Neotectonics of Hispaniola; plate motion, sedimentation, and seismicity at a restraining bend: Earth Planetary Science Letters, v. 70, p. 311 – 324.

Mann, P., Calais, E., Ruegg, J.C., DeMets, C., Jansma, P. & Mattioli, G.S. (2002). Oblique collision in the northeastern Caribbean from GPS measurements and geological observations, Tectonics, 37, doi:0.1029/2001TC001304.

Mann, P., Hippolyte, J.-C., Grindlay, N.R. (2005). Neotectonics of southern Puerto Rico and its offshore margin. In: Geol. Soc. Am., Special Paper 385. 173–214.

Mann, P., DeMets, C., & Wiggins-Grandison, M. (2007). Toward a better understanding of the Late Neogene strike-slip restraining bend in Jamaica: geodetic, geological, and seismic constraints. Geological Society, London, Special Publications, 290(1), 239-253.

McNamara, D., Meremonte, M., Maharrey, J. Z., Mildore, S. L., Altidore, J. R., Anglade, D., ... & Frankel, A. (2012). Frequency-dependent seismic attenuation within the Hispaniola Island region of the Caribbean Sea. Bulletin of the Seismological Society of America, 102(2), 773-782.

Pagani, M, K Johnson, and J. Garcia-Pelaez (2020a). Modelling subduction sources for probabilistic seismic hazard analysis. In: Geological Society, London, Special Publications 501

Pagani, M., Garcia-Pelaez, J., Gee, R., Johnson, K., Poggi, V., Silva, V., Simionato, M., Styron, R., Viganò, D., Danciu, L. and Monelli, D. (2020b). The 2018 version of the Global Earthquake Model: hazard component. *Earthquake Spectra*, *36*(1_suppl), pp.226-251.

Pagani, M. and Marcellini, A., 2007. Seismic-hazard disaggregation: a fully probabilistic methodology. Bulletin of the Seismological Society of America, 97(5), pp.1688-1701.

Pagani, M., Monelli, D., Weatherill, G., Danciu, L., Crowley, H., Silva, V., Henshaw, P., Butler, L., Nastasi, M., Panzeri, L., Simionato, M., Vigano, D., (2014). OpenQuake Engine: An Open Hazard (and Risk) Software for the Global Earthquake Model. Seismological Research Letters 85, 692– 702. doi:10.1785/0220130087

Pasyanos, M.E., T.G. Masters, G. Laske, and Z. Ma (2014). LITHO1.0: An updated crust and lithospheric model of the Earth, J. Geophys. Res., 119 (3), 2153-2173, DOI: 10.1002/2013JB010626.

Peñarubia, H. C., Johnson, K. L., Styron, R. H., Bacolcol, T. C., Sevilla, W. I. G., Perez, J. S., ... & Allen, T. I. (2020). Probabilistic seismic hazard analysis model for the Philippines. Earthquake Spectra, 36(1_suppl), 44-68.

Pindell J.L. and Kennan L. (2009). Tectonic evolution of the Gulf of Mexico, Caribbean, and northern South America in the mantle reference frame: an update, Geological Society, London, Special Publications 2009; v. 328; p. 1-55 doi: 10.1144/SP328.1

Pubellier, M., Mauffret, A., Leroy, S., Vila, J. M., & Amilcar, H. (2000). Plate boundary readjustment in oblique convergence: Example of the Neogene of Hispaniola, Greater Antilles. Tectonics, 19(4), 630-648.

Rodríguez-Zurrunero A., J.L. Granja-Bruña, A. Muñoz-Martín, S. Leroy, U. ten Brink, J.M. Gorosabel-Araus, L. Gómez de la Peña, M. Druet, A. Carbó-Gorosabel (2020). Along-strike segmentation in the northern Caribbean plate boundary zone (Hispaniola sector): Tectonic implications, Tectonophysics (2018), https://doi.org/10.1016/ j.tecto.2020.228322

Saint Fleur, N., Feuillet, N., Grandin, R., Jacques, E., Weil-Accardo, J., and Klinger, Y. (2015). Seismotectonics of southern Haiti: A new faulting model for the 12 January 2010 M7.0 earthquake, Geophys. Res. Lett., 42, 10273–10281, https://doi.org/10.1002/2015GL065505.

Scherbaum F, Cotton F, Smit P (2004). On the use of response spectral-reference data for the selection and ranking of ground-motion models for seismic-hazard analysis in regions of moderate seismicity: the case of rock motion. Bull Seism Soc Am 94(6): 2164–2185

Schorlemmer, D., Gerstenberger, M. C., Wiemer, S., Jackson, D. D., & Rhoades, D. A. (2007). Earthquake likelihood model testing. Seismological Research Letters, 78(1), 17-29.

Schorlemmer, D., Zechar, J. D., Werner, M. J., Field, E. H., Jackson, D. D., Jordan, T. H., & RELM Working Group. (2010). First results of the regional earthquake likelihood models experiment. In Seismogenesis and Earthquake Forecasting: The Frank Evison Volume II (pp. 5-22). Springer, Basel.

Strasser, F. O., M. C. Arango, and J. J. Bommer (2010). Scaling of the Source Dimensions of Interface and Intraslab Subduction-zone Earthquakes with Moment Magnitude. In: Seismological Research Letters 81, pages 941–950.

Styron, R. and García-Pelaez, J. and Pagani, M. (2020). CCAF-DB: The Caribbean and Central American Active Fault Database, Nat. Hazards Earth Syst. Sci. Discuss., 1-42, https://doi.org/10.5194/nhess-2019-46

Styron, R, and Pagani, M. (2020). The GEM Global Active Faults Database." Earthquake Spectra, 36, no. 1_suppl, 160 –180, doi:10.1177/8755293020944182.

Symithe, S., Calais, E., de Chabalier, J.-B., Robertson, R., Higgins, M. (2015). Current block motions and strain accumulation on active faults in the Caribbean. J. Geophys. Res. 120, 1–27.

Terrier-Sedan, M., & Bertil, D. (2021). Active fault characterization and seismotectonic zoning of the Hispaniola island. Journal of Seismology, 25(2), 499-520.

Uhrhammer, R. (1986). Characteristics of Northern and Central California Seismicity, Earthquake Notes, 57(1): 21

Weatherill, G. A. (2014). OpenQuake Ground Motion Toolkit - User Guide. Global EarthquakeModel (GEM). Technical Report.

Weatherill, G., Pagani, M. and Garcia, J. (2016). Exploring Earthquake Databases for the Creation of Magnitude-Homogeneous Catalogues: Tools for Application on a Regional and Global Scale, Geophysical Journal International 206 (3), 1652-1676.

Weichert, D. H. (1980). Estimation of the Earthquake Recurrence Parameters for Unequal Observation Periods for Different Magnitudes. In: Bulletin of the Seismological Society of America 70.4, pages 1337 –1346

Wells, D. L., & Coppersmith, K. J. (1994). New empirical relationships among magnitude, rupture length, rupture width, rupture area, and surface displacement. Bulletin of the seismological Society of America, 84(4), 974-1002.

Youngs, R. R. and K. J. Coppersmith (1985). Implications of fault slip rates and earthquake recurrence models to probabilistic seismic hazard estimates. In: Bull. Seism. Soc. Am. 75.4, pages 939–964

Zechar, J. D., Gerstenberger, M. C., & Rhoades, D. A. (2010). Likelihood-based tests for evaluating space–rate–magnitude earthquake forecasts. Bulletin of the Seismological Society of America, 100(3), 1184-1195.

Zhao, J. X., Zhang, J., Asano, A., Ohno, Y., Oouchi, T., Takahashi, T., Ogawa, H., Irikura, K., Thio, H. K., Somerville, P. G., Fukushima, Y., and Fukushima, Y. (2006). Attenuation relations of strong ground motion in Japan using site classification based on predominant period. Bulletin of the Seismological Society of America, 96(3), 898–913.